Nonreciprocal Microwave Signal Processing with a Field-Programmable Josephson Amplifier

F. Lecocq,[1,*] L. Ranzani,[2] G. A. Peterson,[1] K. Cicak,[1] R. W. Simmonds,[1] J. D. Teufel,[1] and J. Aumentado[1,†]

[1]*National Institute of Standards and Technology, 325 Broadway, Boulder, Colorado 80305, USA*
[2]*Raytheon BBN Technologies, 10 Moulton Street, Cambridge, Massachusetts 02138, USA*

We report on the design and implementation of a field-programmable Josephson amplifier (FPJA)—a compact and lossless superconducting circuit that can be programmed *in situ* by a set of microwave drives to perform reciprocal and nonreciprocal frequency conversion and amplification. In this work, we demonstrate four modes of operation: frequency conversion (transmission of -0.5 dB, reflection of -30 dB), circulation (transmission of -0.5 dB, reflection of -30 dB, isolation of 30 dB), phase-preserving amplification (gain > 20 dB, one photon of added noise) and directional phase-preserving amplification (reflection of -10 dB, forward gain of 18 dB, reverse isolation of 8 dB, one photon of added noise). The system exhibits quantitative agreement with the theoretical prediction. Based on a gradiometric superconducting quantum-interference device with $Nb/Al\text{-}AlO_x/Nb$ Josephson junctions, the FPJA is first-order insensitive to flux noise and can be operated without magnetic shielding at low temperature. Owing to its flexible design and compatibility with existing superconducting fabrication techniques, the FPJA offers a straightforward route toward on-chip integration with superconducting quantum circuits such as qubits and microwave optomechanical systems.

I. INTRODUCTION

Many superconducting quantum circuits rely on microwave photons to measure or couple quantum systems, such as superconducting qubits or micromechanical resonators [1,2]. The ability to process microwave fields with minimal degradation is crucial to the observation of truly quantum behavior. For example, quantum-limited amplification maximizes measurement fidelity, a crucial metric in quantum computing [1,3,4], quantum feedback [5–7], the observation of quantum trajectories [8], and position measurements [9]. Similarly, the efficient routing of microwave photons enables long-distance entanglement [10] and is an important tool in proposals for quantum networks [11].

Recent developments in Josephson-junction-based parametric amplifiers have led to an order of magnitude improvement in measurement efficiency compared to commercially available high-electron-mobility-transistor (HEMT) amplifiers [12–14]. However, these amplifiers are *reciprocal* devices; i.e., their scattering parameter amplitudes are symmetric under the exchange of source and detector [15–17]. As a consequence, in order to protect the device under test from amplifier backaction and to control signal flow, they require the use of microwave circulators to separate input signals from amplified output onto different physical ports. These components drastically reduce quantum measurement efficiencies [18,19]. In

addition to their intrinsic loss, circulators are relatively large and require large dc magnetic fields, preventing direct integration into modern superconducting circuits.

The limitations outlined above have motivated the development of nonreciprocal, nonmagnetic, lossless circuits [16,17,20–27]. Many of these approaches seek to provide highly efficient routing or amplification solutions that can be tightly integrated with superconducting circuits. For example, Josephson traveling-wave parametric amplifiers were specifically designed to achieve high directional gain over several gigahertz of bandwidth, with a large dynamic range [27]. In this work, we demonstrate a wider range of nonreciprocal behavior, using parametrically coupled multimode circuits to build an interferometer in frequency space [16,17]. Owing to the directional phase shift inherent in parametric interactions, different interferences occur in the forward and backward directions. Complex networks of coupled modes can be programmed *in situ* by choosing a set of applied parametric microwave drives, leading to a variety of nonreciprocal scattering parameters. The versatility of this approach was recently demonstrated in a Josephson parametric converter [26]. In this work, we present an alternative circuit design, based on lumped-element niobium components coupled via a single gradiometric superconducting quantum-interference device (SQUID), insensitive to flux noise. Experimental measurements of both the scattering parameters and noise performance show quantitative agreement with theoretical calculations. Here, we focus on cases in which two or three modes are coupled and demonstrate four basic functions: frequency conversion, circulation, phase-preserving amplification, and directional phase-preserving amplification. In the following, we discuss the device and

*Corresponding author.
florent.lecocq@nist.gov
†Corresponding author.
jose.aumentado@nist.gov

measurement setup and then describe each mode of operation. Detailed calculations, noise calibrations, and device fabrication details are given in the appendixes.

II. DESCRIPTION OF THE FIELD-PROGRAMMABLE JOSEPHSON AMPLIFIER (FPJA)

The device shown in Fig. 1 consists of three lumped-element resonant circuits in parallel connected to a single SQUID. The SQUID acts as a tunable linear inductor that can be modulated at microwave frequencies. The device is mounted in a dilution refrigerator and measured in reflection; see Fig. 1(a). The scattering parameters are measured using a vector network analyzer with a frequency-conversion option. A separate broadband pump line is used to thread flux through the SQUID loop. The circuit exhibits resonances at three frequencies, ω_a, ω_b, and ω_c. Each of these resonances shows a dependence on the SQUID inductance which is, in turn, modulated by the applied SQUID flux Φ, as shown in Fig. 1(b). The circuit components are designed to place all three resonances within the 4-GHz to 8-GHz band, while ensuring that all of the possible frequency combinations $\omega_j \pm \omega_k$, where j, $k \in \{a, b, c\}$, are well separated—a critical property for well-controlled parametric interactions (see Appendix B). Coupling capacitors to ground and to the 50-Ω environment set the external coupling rates to the single measurement line, κ_j^{ext}. The use of a low-loss dielectric for the capacitors (amorphous silicon, loss tangent $\lesssim 5 \times 10^{-4}$) ensures that these rates exceed the internal loss rates κ_j^{int} by more than an order of magnitude and dominate the total

linewidths $\kappa_j = \kappa_j^{\text{ext}} + \kappa_j^{\text{int}}$. In the following, we fix the dc flux bias to $\Phi/\Phi_0 \approx 0.29$, where Φ_0 is a flux quantum, and the measured frequencies and linewidths are summarized in Fig. 1(c).

III. OPERATION OF THE FPJA

Currents from the three resonators of the FPJA flow through the SQUID, effectively linearly coupling their dynamics. These dynamics occur at vastly different frequencies and, to first order, they can be treated independently. However, the modulation of the coupling element, here the SQUID inductance, can lead to parametric coupling between the resonators [28,29], as discussed in Appendix B. In the presence of such a *pump*, the time-dependent coupling strength between the modes j and k is

$$g_{jk}(t) = \frac{\delta\Phi_{jk}(t)}{4}\sqrt{\frac{\partial\omega_j}{\partial\Phi}\frac{\partial\omega_k}{\partial\Phi}}, \tag{1}$$

where $\delta\Phi_{jk}(t) = |\delta\Phi_{jk}|\cos(\omega_{jk}^p t + \phi_{jk})$ is the flux modulation with an amplitude $|\delta\Phi_{jk}|$, a frequency ω_{jk}^p, and a phase ϕ_{jk}. The coupling term in the Hamiltonian of the system depends on the modulation frequency. Specifically, the pump can mediate two kinds of parametric coupling between two modes. For pump frequencies of the form $|\omega_j - \omega_k|$, where $j, k \in \{a, b, c\}$, the creation or annihilation of a pump photon enables the coherent exchange of a photon between the modes j and k, leading to frequency conversion. For pump frequencies of the form $\omega_j + \omega_k$, the annihilation of a pump photon creates a correlated pair of photons in the modes j and k, leading to amplification. Importantly, multiple pumps can be simultaneously applied to program an arbitrary set of coupling terms between the modes. A network of modes and couplings can be built, defining the behavior of the circuit. We utilize a graph-based analysis [16] that emphasizes the topology of the coupling network, which is crucial to building intuition and leads to a good agreement with the data. The general methodology consists of solving the Heisenberg-Langevin coupled equations of motion (EOM) of the circuit for a given pump configuration. Using input-output formalism, we calculate the scattering parameters and the output noise of the system. Detailed calculations are available in Appendix B.

A. The FPJA as a frequency converter

We start with the first building block: frequency conversion between two modes—here chosen to be a and b. We modulate the flux through the SQUID with a pump at a frequency $\omega_{ab}^p \approx |\omega_b - \omega_a|$. An input signal of amplitude a_{in}, driving the mode amplitude a at a frequency ω_a^s, is coupled to the mode amplitude b, leading to an output signal of amplitude b_{out} at a frequency $\omega_b^s = \omega_a^s + \omega_{ab}^p$, and vice versa [see Fig. 2(a)]. The EOMs in the signal frame reduce to
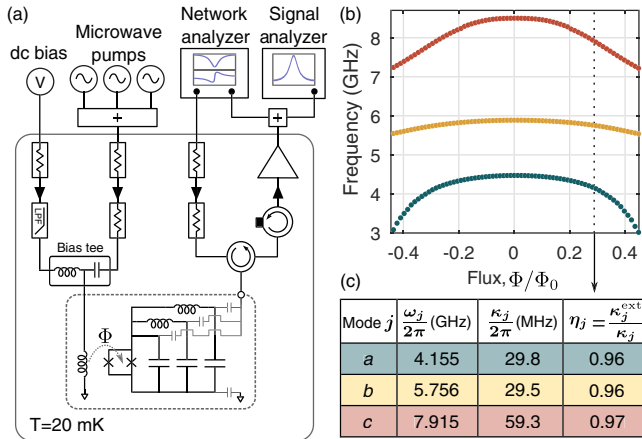

FIG. 1. Device and experimental setup. (a) A superconducting resonant circuit is measured in reflection in a cryostat (LPF: low-pass filter). It exhibits three resonances whose frequencies are tunable by the flux applied to a single SQUID. (b) Measured resonance frequencies ω_a, ω_b, and ω_c, as a function of the flux bias to the SQUID. (c) Table of device parameters for $\Phi/\Phi_0 \approx 0.29$, showing the resonance frequency ω_j, the total linewidth κ_j, and the coupling efficiency $\eta_j = \kappa_j^{\text{ext}}/\kappa_j$ of each mode j.

Mode j	$\frac{\omega_j}{2\pi}$ (GHz)	$\frac{\kappa_j}{2\pi}$ (MHz)	$\eta_j = \frac{\kappa_j^{\text{ext}}}{\kappa_j}$
a	4.155	29.8	0.96
b	5.756	29.5	0.96
c	7.915	59.3	0.97

$$\kappa_a \Delta_a a + \sqrt{\kappa_a \kappa_b} \beta_{ab} b = i \sqrt{\kappa_a^{\text{ext}}} a_{\text{in}},$$

$$\kappa_b \Delta_b b + \sqrt{\kappa_a \kappa_b} \beta_{ab}^* a = i \sqrt{\kappa_b^{\text{ext}}} b_{\text{in}}, \qquad (2)$$

with $\Delta_j = (\omega_j^s - \omega_j)/\kappa_j + i/2$ being the normalized detuning for mode j and $\beta_{ab} = |g_{ab}| e^{i\phi_{ab}}/(2\sqrt{\kappa_a \kappa_b})$ the normalized coupling between the mode amplitudes a and b. Importantly, this coupling term is complex, with its phase ϕ_{ab} and amplitude $|g_{ab}|$ inherited from the pump. We show in Fig. 2(b) a graph representation of the EOMs in Eq. (2), where vertices represent the mode amplitude and arrows represent the detuning and coupling terms. In the ideal resonant case, defined as $\omega_{ab}^p = |\omega_b - \omega_a|$ and $\omega_j^s = \omega_j$, and neglecting internal loss, $\kappa_j^{\text{int}} = 0$, the scattering matrix $\mathbf{S}$ for the system is

$$\mathbf{S} = \begin{pmatrix} \frac{1-4|\beta_{ab}|^2}{1+4|\beta_{ab}|^2} & \frac{4i\beta_{ab}}{1+4|\beta_{ab}|^2} \\ \frac{4i\beta_{ab}^*}{1+4|\beta_{ab}|^2} & \frac{1-4|\beta_{ab}|^2}{1+4|\beta_{ab}|^2} \end{pmatrix}. \qquad (3)$$

Close examination of the scattering matrix reveals that unity transmission coincides with impedance matching (zero reflection) at $|\beta_{ab}| = 1/2$, and the corresponding signal-flow diagram [30] is shown in Fig. 2(c). We note here that
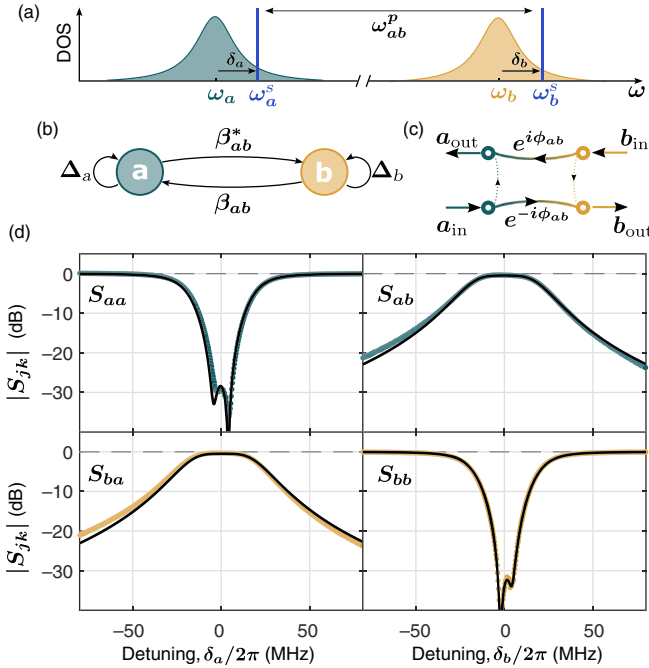

FIG. 2. Frequency converter. (a) Frequency-space diagram. A strong pump of frequency $\omega_{ab}^p = |\omega_b - \omega_a|$ converts an input signal at the frequency $\omega_a^s = \omega_a + \delta_a$ to a output signal frequency $\omega_b^s = \omega_b + \delta_b$, and vice versa. (b) Graph representation of the EOM (2). (c) Ideal signal-flow diagram. (d) Measured scattering parameters (the dots) and fits to Eq. (2) (the lines), for a fixed pump strength $|\beta_{ab}| \approx 0.5$, as a function of the detuning δ_j. The device exhibits good impedance matching (low return loss) and near-unity transmission.

$S_{ba} = -S_{ab}^*$, naively providing gyration. While this relation will be crucial later for establishing directionality, on its own it is not unconditionally nonreciprocal due to an ambiguity in the reference frame when describing scattering between two different frequency modes [15,16,31].

The measured scattering parameters in our device are shown in Fig. 2(d) as a function of the detuning $\delta_j = \omega_j^s - \omega_j$. We fit the measured response using the full solutions of Eq. (2), finding very good agreement with the data. Specifically, we measure only 0.5 dB of insertion loss, fully captured by including the internal loss of the resonators so that $|S_{ba}|^2 = \kappa_a^{\text{ext}} \kappa_b^{\text{ext}}/\kappa_a \kappa_b$ (see Appendix B). The circuit is well matched, with 30 dB of return loss. The bandwidth of conversion is $\sqrt{\kappa_a \kappa_b}/2\pi \approx 30$ MHz.

B. The FPJA as a two-mode amplifier

We now describe the second building block: amplification between two modes—here chosen to be a and b. We modulate the flux through the SQUID with a pump at the sum frequency $\omega_{ab}^p \approx \omega_b + \omega_a$. An input signal at a frequency ω_a^s is amplified and generates an idler at $-\omega_b^s = \omega_a^s - \omega_{ab}^p$ [see Fig. 3(a)]. In contrast to the frequency-conversion case in Eq. (2), the dynamics of the mode amplitude a are now coupled to the conjugate-mode amplitude b^*, and the EOMs in the signal frame reduce to

$$\kappa_a \Delta_a a + \sqrt{\kappa_a \kappa_b} \beta_{ab} b^* = i \sqrt{\kappa_a^{\text{ext}}} a_{\text{in}},$$

$$-\kappa_b \Delta_b^* b^* - \sqrt{\kappa_a \kappa_b} \beta_{ab}^* a = i \sqrt{\kappa_b^{\text{ext}}} b_{\text{in}}^*, \qquad (4)$$

with $\Delta_j = (\omega_j^s - \omega_j)/\kappa_j + i/2$ and $\beta_{ab} = |g_{ab}| e^{-i\phi_{ab}}/(2\sqrt{\kappa_a \kappa_b})$. Again, when making a comparison with the frequency-conversion case, one can notice the sign change for the detuning term and the coupling term in the equation for b^*. These subtle differences lead to a very different scattering matrix $\mathbf{S}$, which, in the ideal resonant case ($\omega_{ab}^p = \omega_b + \omega_a$ and $\omega_j^s = \omega_j$) and neglecting internal loss ($\kappa_j^{\text{int}} = 0$), is

$$\mathbf{S} = \begin{pmatrix} \frac{1+4|\beta_{ab}|^2}{1-4|\beta_{ab}|^2} & \frac{4i\beta_{ab}}{1-4|\beta_{ab}|^2} \\ \frac{-4i\beta_{ab}^*}{1-4|\beta_{ab}|^2} & \frac{1+4|\beta_{ab}|^2}{1-4|\beta_{ab}|^2} \end{pmatrix}. \qquad (5)$$

Close examination of the scattering matrix in Eq. (5) reveals a divergence for $|\beta_{ab}| = 1/2$, in stark contrast to the frequency-conversion case [Eq. (3)]. In the limit $|\beta_{ab}| \to 1/2^-$, each scattering parameter has an amplitude gain related to $\sqrt{G} \approx 2/(1 - 4|\beta_{ab}|^2)$, and the full signal flow is shown in Fig. 3(c). As in the frequency-conversion case, note that $S_{ba} = S_{ab}^*$. In Fig. 3(d), we show the measured scattering parameters for various values of $|\beta_{ab}|$, i.e., for various pump powers. As $|\beta_{ab}|$ increases, so too does the gain, at the expense of a typical reduction in linewidth [32]. Good agreement is found with a fit to the solutions of Eq. (4).
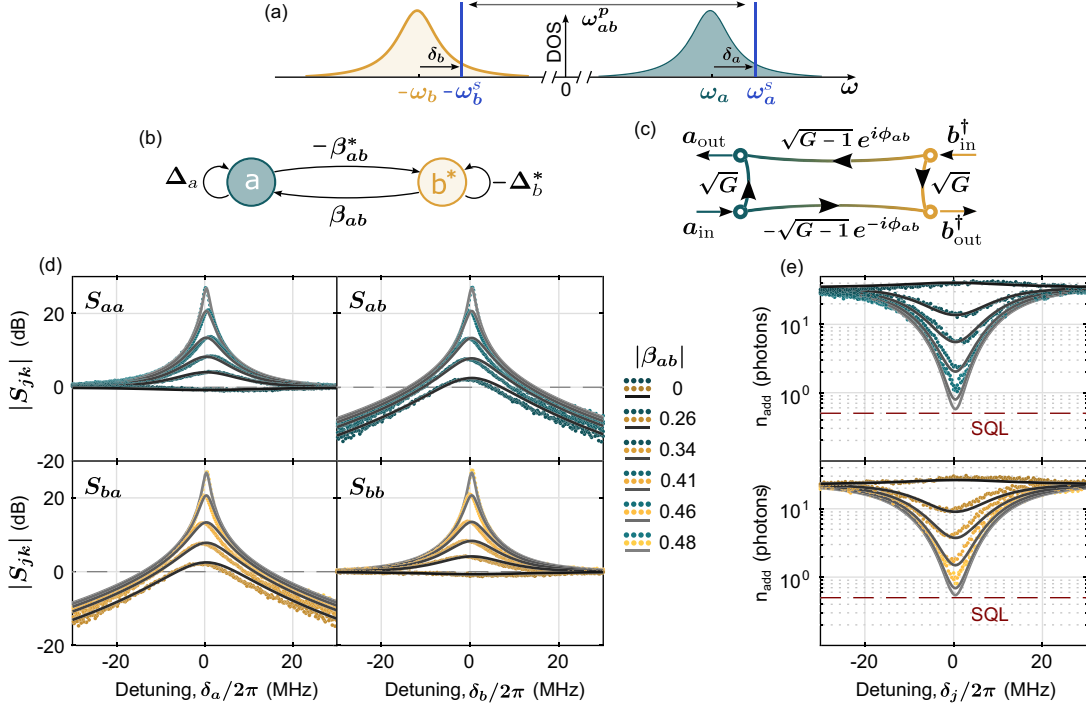
FIG. 3. Two-mode amplifier. (a) Frequency-space diagram. A strong pump of frequency $\omega_{ab}^p = \omega_b + \omega_a$ amplifies an input signal at the frequency $\omega_a^s = \omega_a + \delta_a$ and generates an idler at the frequency $-\omega_b^s = -\omega_b + \delta_b$, and vice versa. (b) Graph representation of the EOM (4). (c) Ideal signal-flow diagram. (d) Measured scattering parameters (the dots) and fits to Eq. (4) (the lines), as a function of the detuning δ_j, for the increasing pump strength β_{ab} (from dark to light color). (e) Measured system-added noise (the dots) and theoretical predictions (the lines) referred to the input of the FPJA, as a function of the detuning δ_j.

The noise performance of the amplifier is shown in Fig. 3(e), and additional details can be found in Appendix C. In a separate experiment, we calibrate an upper bound for the system-added noise of the measurement setup at the reference plane of the FPJA, allowing us to convert the noise floor into photon units. The system-added noise referred to the input of the FPJA is then obtained by dividing the output noise by the measured gain. For $|\beta_{ab}| = 0$, the internal loss of the resonators acts as an attenuator and we observe a slight degradation of the system-added noise, up to $n_{\mathrm{add}} \approx 40$ photons at ω_a and $n_{\mathrm{add}} \approx 30$ photons at ω_b. As the gain increases, the noise contribution of the measurement chain is overwhelmed and the system-added noise decreases, down to $n_{\mathrm{add}} \approx 1.0 \pm 0.1$ photons at ω_a and ω_b, approaching the standard quantum limit (SQL) of $n_{\mathrm{add}}^{\mathrm{SQL}} = 0.5$. The system-added noise plateaus at high gain, remaining slightly above the SQL. This limit could originate from excess thermal population of the resonators or potential excess loss in the FPJA packaging—or simply from an offset in the reference plane of the noise calibration.

C. The FPJA as a circulator

By connecting all three resonators via frequency conversion, we can build the first nontrivial mode of operation: the circulator. Using three pumps, we modulate the flux through the SQUID at the difference frequencies

$\omega_{jk} \approx |\omega_j - \omega_k|$, where j, $k \in \{a, b, c\}$, satisfying the condition $\omega_{ab}^p + \omega_{bc}^p = \omega_{ac}^p$ [see Fig. 4(a)]. Effectively, these pumps form a closed loop in frequency space connecting the input and output signals at ω_j^s, where $j \in \{a, b, c\}$. The EOMs in the signal frame reduce to

$$\kappa_a \Delta_a a + \sqrt{\kappa_a \kappa_b} \beta_{ab} b + \sqrt{\kappa_a \kappa_c} \beta_{ac}^* c = i\sqrt{\kappa_a^{\mathrm{ext}}} a_{\mathrm{in}},$$

$$\kappa_b \Delta_b b + \sqrt{\kappa_b \kappa_c} \beta_{bc} c + \sqrt{\kappa_a \kappa_b} \beta_{ab}^* a = i\sqrt{\kappa_b^{\mathrm{ext}}} b_{\mathrm{in}},$$

$$\kappa_c \Delta_c c + \sqrt{\kappa_a \kappa_c} \beta_{ac} a + \sqrt{\kappa_b \kappa_c} \beta_{bc}^* b = i\sqrt{\kappa_c^{\mathrm{ext}}} c_{\mathrm{in}}, \quad (6)$$

with $\Delta_j = (\omega_j^s - \omega_j)/\kappa_j + i/2$ and $\beta_{jk} = |g_{jk}|e^{i\phi_{jk}}/(2\sqrt{\kappa_j \kappa_k})$, where j, $k \in \{a, b, c\}$. The graph representation of this equation is shown in Fig. 4(b). This loop topology is at the heart of the nonreciprocal behavior of this mode of operation. Indeed, by closing this loop, we build an interferometer, where the phase shift in each arm is direction dependent. The interference is controlled by the loop phase $\phi_{\mathrm{loop}} = \phi_{ab} + \phi_{bc} - \phi_{ac}$, where ϕ_{jk} is the phase of the pump connecting modes j and k. In the ideal resonant case $\omega_{jk} = |\omega_j - \omega_k|$ and $\omega_j^s = \omega_j$, neglecting internal loss, tuning each coupling strength to produce the ideal frequency conversion ($|\beta_{jk}| = 1/2$), and, for $\phi_{\mathrm{loop}} = -\pi/2$, the scattering matrix **S** for the system is
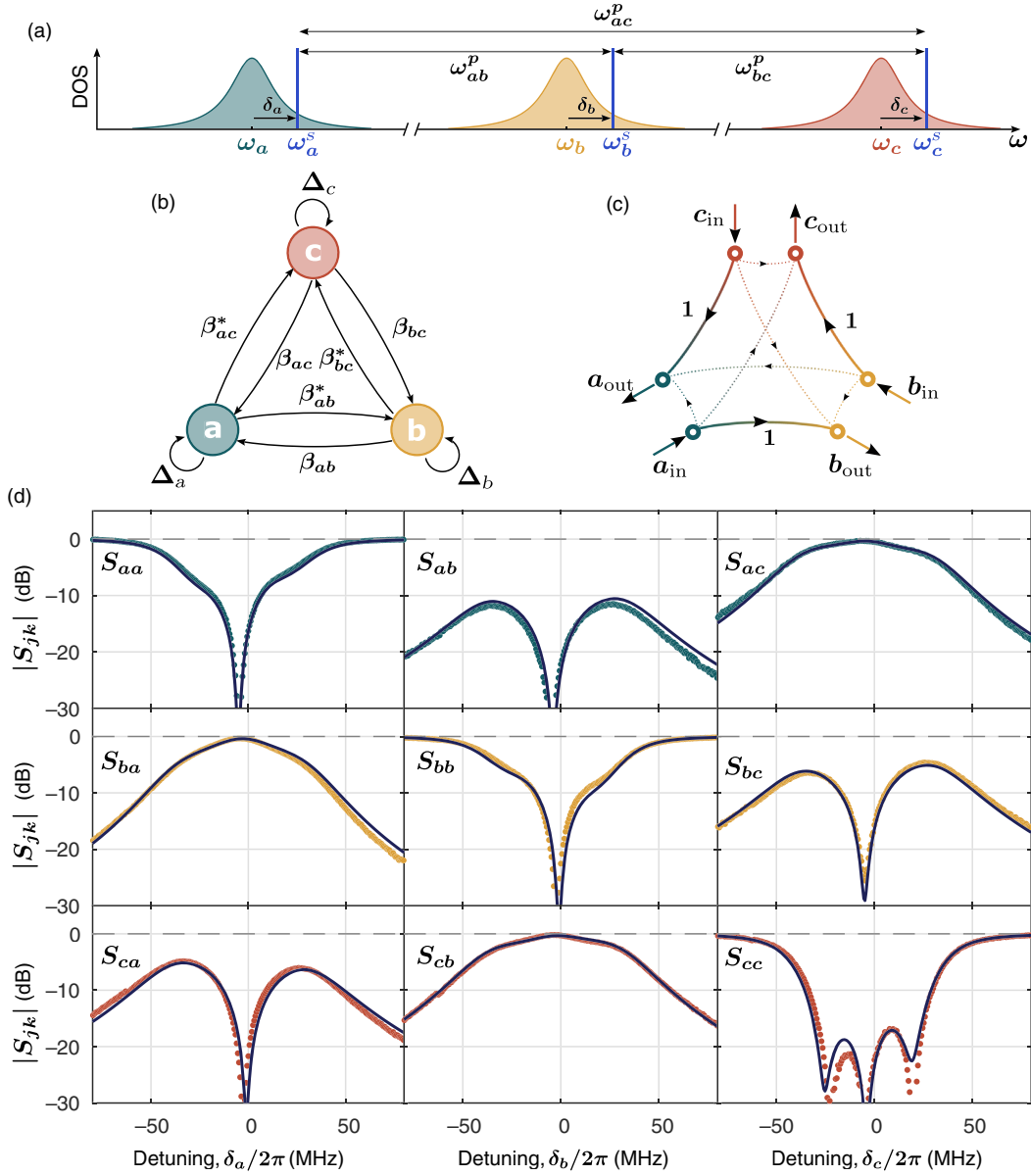
FIG. 4.   Circulator. (a) Frequency-space diagram. Three pumps, with the frequencies $\omega_{ab}^p \approx |\omega_b - \omega_a|$, $\omega_{bc}^p \approx |\omega_c - \omega_b|$, $\omega_{ac}^p \approx |\omega_c - \omega_a|$ and the respective phases ϕ_{ab}, ϕ_{bc}, and ϕ_{ac}, allow a conversion between signals at the frequencies $\omega_j^s = \omega_j - \delta_j$ ($j \in \{a, b, c\}$), closing a loop in frequency space. Interference between paths enables nonreciprocal signal circulation. The circulation direction is set by the total loop phase, $\phi_{\text{loop}} = \phi_{ab} + \phi_{bc} - \phi_{ac}$. (b) Graph representation of the EOM (6). (c) Ideal signal-flow diagram. (d) Measured scattering parameters (the dots) and fits to Eq. (6) (the lines), as a function of the detuning δ_j, for fixed pump powers ($|\beta_{jk}| = 1/2$) and loop phase ($\phi_{\text{loop}} \approx -\pi/2$).

$$\mathbf{S} = \begin{pmatrix} 0 & 0 & 1 \\ 1 & 0 & 0 \\ 0 & 1 & 0 \end{pmatrix}. \tag{7}$$

In this case, the system is matched, with $|S_{jj}| = 0$, and nonreciprocal, $|S_{jk}| \neq |S_{kj}|$, corresponding to the signal-flow diagram in Fig. 4(c). An input signal in mode a circulates to mode b and then c. The direction of circulation is controlled by the loop phase and can be reversed by setting $\phi_{\text{loop}} = \pi/2$.

Experimentally, we start by tuning the pumps to produce ideal frequency conversion between each pair of modes separately, and then we simultaneously turn on all three pumps. The measured scattering parameters for $\phi_{\text{loop}} = -\pi/2$ are shown in Fig. 4(d). The full dependence with the loop phase ϕ_{loop} is shown in Fig. 8. Very good agreement is obtained with the solutions of Eq. (6). With the return loss exceeding 20 dB, the device exhibits an excellent impedance match at all three modes. We measure a transmission efficiency of more than -0.5 dB and an isolation exceeding 20 dB over a 6-MHz bandwidth. A transmission efficiency

of more than -1 dB and an isolation exceeding 10 dB is maintained over a 60-MHz bandwidth.

D. The FPJA as a directional amplifier

When operated as a two-mode amplifier, the FPJA is nondirectional (see Fig. 3), and it requires a circulator to separate the input and output signals. In this section, we circumvent this requirement by operating the FPJA as a directional amplifier. Using three pumps, we modulate the flux through the SQUID at the frequencies $\omega_{ac}^p \approx \omega_c - \omega_a$, $\omega_{ab}^p \approx \omega_b + \omega_a$, and $\omega_{bc}^p \approx \omega_c + \omega_b$, satisfying the overall loop closure condition $\omega_{ac}^p + \omega_{ab}^p = \omega_{bc}^p$ [see Fig. 5(a)].

This pump configuration corresponds to simultaneously connecting modes a and c via frequency conversion while connecting modes a and b and modes b and c via amplification, forming a loop in frequency space. The resulting EOMs are

$$\kappa_a \Delta_a a + \sqrt{\kappa_a \kappa_b}\beta_{ab} b^* + \sqrt{\kappa_a \kappa_c}\beta_{ac} c = i\sqrt{\kappa_a^{\text{ext}}} a_{\text{in}},$$

$$-\kappa_b \Delta_b^* b^* + \sqrt{\kappa_b \kappa_c}\beta_{bc} c - \sqrt{\kappa_a \kappa_b}\beta_{ab}^* a = i\sqrt{\kappa_b^{\text{ext}}} b_{\text{in}}^*,$$

$$\kappa_c \Delta_c c + \sqrt{\kappa_a \kappa_c}\beta_{ac}^* a - \sqrt{\kappa_b \kappa_c}\beta_{bc}^* b^* = i\sqrt{\kappa_c^{\text{ext}}} c_{\text{in}}. \qquad (8)$$
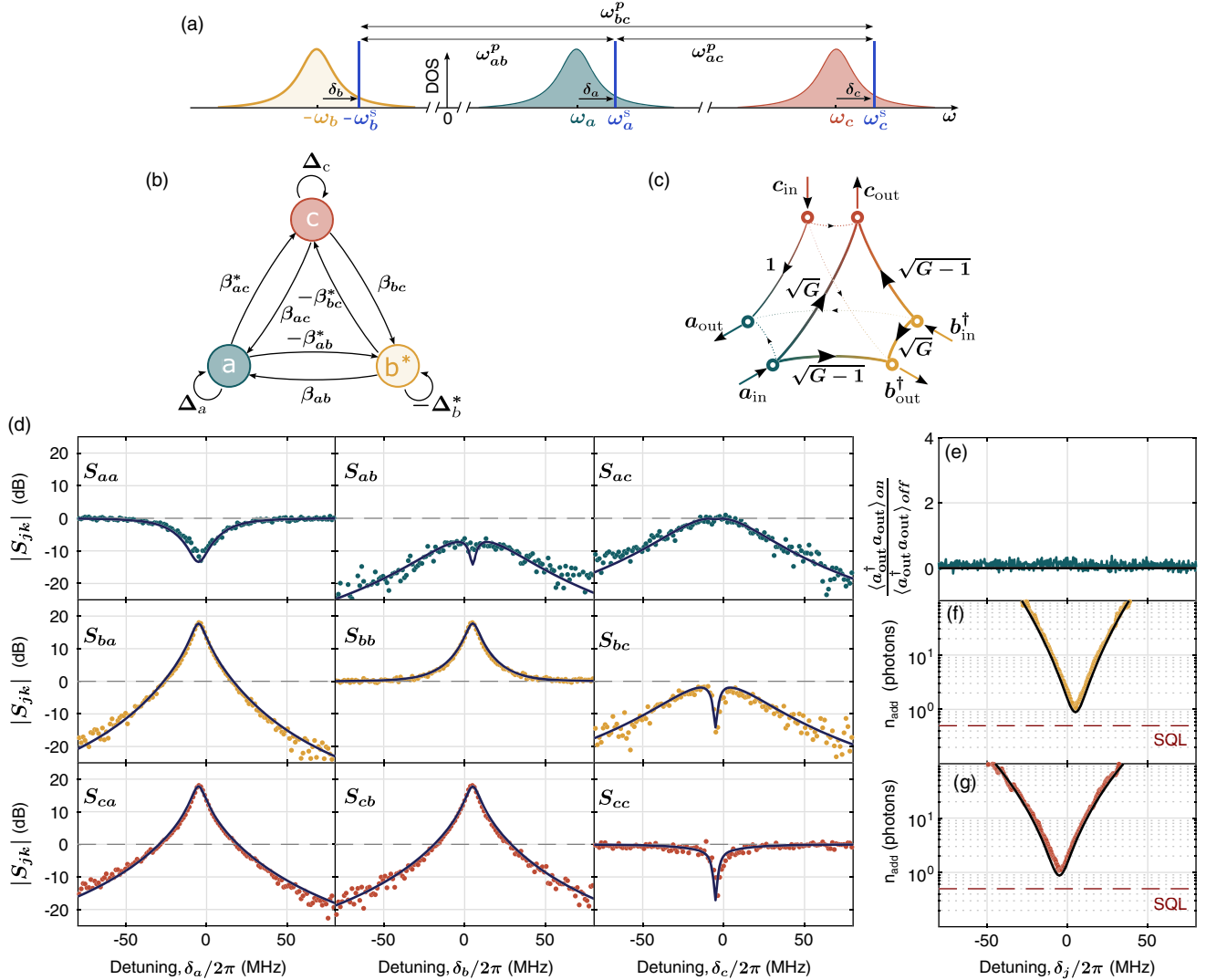

FIG. 5.   Directional phase-preserving amplifier. (a) Frequency-space diagram. Three pumps, with the frequencies $\omega_{ac}^p \approx |\omega_c - \omega_a|$, $\omega_{ab}^p \approx \omega_b + \omega_a$, and $\omega_{bc}^p \approx \omega_c + \omega_b$ and the respective phases ϕ_{ab}, ϕ_{bc}, and ϕ_{ac}, allow a conversion between signals at the frequencies ω_a^s, $-\omega_b^s$ and ω_c^s, closing a loop in frequency space. Interferences between paths enable nonreciprocal signal amplification. The amplification direction is set by the total loop phase, $\phi_{\text{loop}} = \phi_{ab} + \phi_{bc} + \phi_{ac}$. (b) Graph representation of the EOM (8). (c) Ideal signal-flow diagram. (d) Measured scattering parameters (the dots) and fits to Eq. (8) (the lines) as a function of the detuning δ_j, for fixed pump powers ($|\beta_{jk}| \approx 1/2$) and loop phase ($\phi_{\text{loop}} \approx -\pi/2$). (e) Return noise of the amplifier. Ratio of the measured noise power out of mode a for the pumps on and off, showing that no extraneous noise is added by the amplifier. (f),(g) Measured system-added noise (the dots) and theoretical predictions (the lines) referred to the input of the FPJA, as a function of the detuning δ_j, for modes b and c, respectively.

The graph representation of these EOMs is shown in Fig. 5(b). As in the circulator case, the loop phase $\phi_{\text{loop}} = \phi_{ab} + \phi_{bc} + \phi_{ac}$ controls the directionality of the device. In the ideal resonant case, neglecting internal loss, tuning coupling strength to produce ideal frequency conversion between modes a and c, $|\beta_{ac}| = 1/2$, for symmetric amplification coupling strength $|\beta_{ab}| = |\beta_{bc}|$ and for $\phi_{\text{loop}} = -\pi/2$, the scattering matrix $\mathbf{S}$ is

$$\mathbf{S} = \begin{pmatrix} 0 & 0 & 1 \\ \sqrt{G-1} & \sqrt{G} & 0 \\ \sqrt{G} & \sqrt{G-1} & 0 \end{pmatrix}, \qquad (9)$$

where $\sqrt{G} = (1 + 4|\beta_{ab}|^2)/(1 - 4|\beta_{ab}|^2)$. In this configuration, mode a serves as the input port and is impedance matched (no reflection). An input signal is amplified toward both output modes b and c. The amplified signal at each output is added to the amplified vacuum seeded into mode b, resulting in the same minimum system-added noise as for a standard two-mode amplifier. Finally, vacuum noise seeded into mode c is routed to mode a with unity gain. The measured scattering parameters for $\phi_{\text{loop}} = \pi/2$ are shown in Fig. 5(d). The full dependence with the loop phase ϕ_{loop} is shown in Fig. 9. Good agreement is obtained with the numerical solutions of Eq. (8). We obtain a forward gain of 18 dB while maintaining good impedance matching (a return loss in excess of 10 dB) and isolation (in excess of 8 dB). The noise performances are shown in Figs. 5(e), 5(f), and 5(g), corresponding to the respective outputs of modes a, b, and c. The system-added noise measured at the outputs of modes b and c, referred to the input of mode a, approach the quantum limit with $n_{\text{add}} \approx 1.1 \pm 0.1$ photons. Moreover, because of the directionality of the amplifier, we do not observe any noise rise at the output of mode a, and we therefore do not expect any backaction on a future device under test— a crucial property for the integrated measurement of a microwave quantum system.

IV. DISCUSSION AND CONCLUSION

The approach presented in this work is compatible with most superconducting quantum-computation systems, opening the way to full integrability and scalability. We note that, to accommodate various devices under test, it would be straightforward to design a circuit with bare resonance frequencies placed between 2 and 20 GHz and linewidths individually set between 5 and 500 MHz. Routing the different mode frequencies to separate physical ports relies on the design of a low-loss on-chip microwave multiplexer, directly compatible with the device fabrication.

Compared to recent work using a Josephson parametric converter (JPC) [26], our approach differs on both the design and technological levels. The JPC exploits a design with a high degree of symmetry to naturally separate the modes to different physical ports and to maximize the dynamic range. The design choices in the FPJA are intended to take advantage of a powerful niobium-based fabrication technology that enables (1) the design of low-loss and compact lumped-element circuits, (2) the fabrication of a high critical current, gradiometric, SQUIDs with on-chip ac and dc flux bias, and (3) the straightforward extension to more complex multimode circuits.

To conclude, we have demonstrated the ability to program *in situ* a low-loss superconducting device to perform reciprocal and nonreciprocal analog microwave signal processing close to the quantum limit. We emphasize that we have shown here only a small subset of all the possible networks of parametrically coupled modes. Other networks, using three or more modes, could, for example, lead to phase-sensitive directional amplification, opening the way to the ideal detection efficiency of microwave signals.

APPENDIX A: DEVICE FABRICATION AND LAYOUT

The device is fabricated with optical lithography by using a Nb/Al-AlO$_x$/Nb trilayer process to form Josephson junctions, and by utilizing amorphous silicon (a-Si) as a low-loss interlayer dielectric. The circuit layout and pictures are shown in Fig. 6. The device fabrication is summarized in Fig. 6(c):

(i) A Nb/Al-AlO$_x$/Nb trilayer is prepared on a high-resistivity intrinsic silicon wafer (>20 kΩ cm) by subsequently sputtering a 200-nm Nb layer (red), an 8-nm Al layer which is then oxidized to form a tunnel barrier (black) and, finally, a 110-nm Nb layer (yellow). The preparation of the trilayer is performed *in situ* in a sputtering deposition tool without breaking vacuum.

(ii) The trilayer is patterned top down in three iterations of optical lithography followed by material etching. First, the Josephson-junction (JJ) areas are defined by etching the top Nb layer (yellow) using a vertical plasma etch (SF$_6$/O$_2$). Second, the excess Al-AlO$_x$ (black) is removed everywhere except around the junctions by a wet etch (MF-26A, which is also the optical resist developer). Finally, we define the bottom wiring layer in Nb (red) using a sloped plasma etch (CF$_4$/O$_2$).

(iii) The Josephson junctions and the bottom wiring layer are covered by a 300-nm amorphous silicon layer (a-Si) deposited by PECVD. Vias are then defined
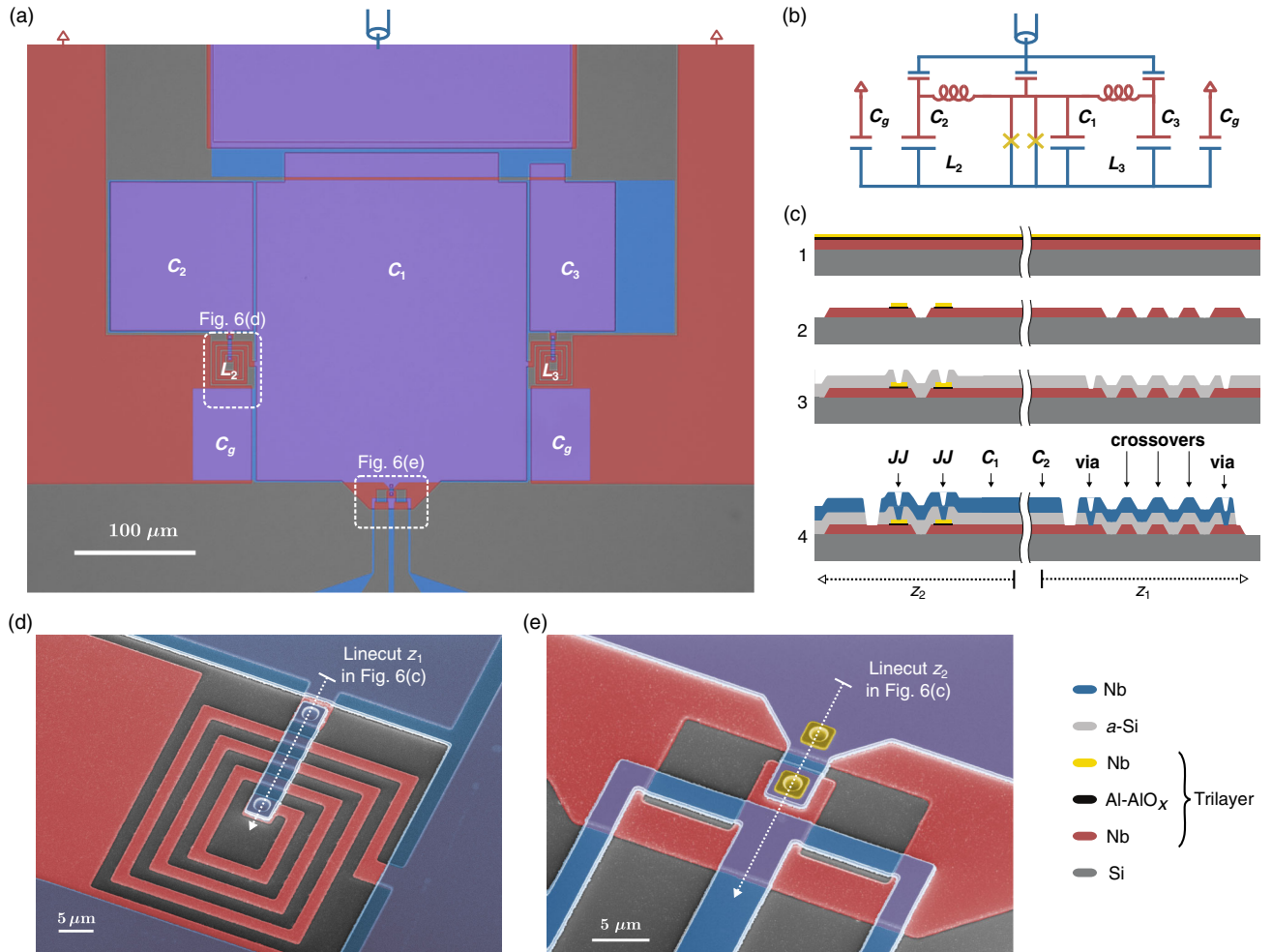
FIG. 6. Device fabrication and layout. (a) False colored optical micrograph. The silicon substrate is in gray, the bottom Nb layer in red, and the top Nb layer in blue. Overlap between the two Nb layers forms parallel-plate capacitors, in purple. (b) Circuit equivalent of the device. (c) Fabrication process, along the cross sections z_1 and z_2 shown in (d) and (e). In step 1, the Nb/Al-AlO$_x$/Nb trilayer is prepared on an intrinsic silicon wafer. In step 2, the trilayer is patterned top down in three steps to define Josephson junctions and the bottom Nb wiring layer. In step 3, the a-Si dielectric layer is deposited and patterned to define vias. In step 4, the Nb layer is deposited over the a-Si and vias, and it is patterned to define the top wiring layer. Any uncovered a-Si is also removed in this step. (d),(e) Scanning electron micrograph of one of the coil inductors, and of the gradiometric SQUID, using the same color scheme, with, additionally, the Josephson junction in yellow.

by etching into the a-Si layer using a sloped plasma etch (SF$_6$/O$_2$).

(iv) After an *in situ* rf clean, a 300-nm Nb layer is sputtered and patterned by a vertical plasma etch (SF$_6$) to define the top wiring layer (blue). This etch also removes any uncovered a-Si.

The properties of the a-Si layer are characterized by independent measurements of lumped-element LC resonators fabricated on the same wafer as the FPJA, yielding a relatively high dielectric constant ($\epsilon_r \approx 9$) and a low loss tangent (1.5–5×10^{-4}). This allows for the design of compact and low-loss lumped-element capacitors and inductors. The Josephson junctions have an area of $2.5 \times 2.5\ \mu$m^2, and the oxidation parameters lead to a critical current of $I_c = 5\ \mu$A per junction. The SQUID

loop has a gradiometric design, first-order insensitive to magnetic fields.

The design of the device is based on a circuit with three discrete poles, each tunable by a single SQUID inductance. The circuit consist of three LC resonators connected in parallel ($L_{SQ}C_1$, L_2C_2, and L_3C_3), as shown in Fig. 6. Alternatively, this device can be understood as two LC resonators, L_2C_2 and L_3C_3, coupled via a resonant coupling element (formed by the SQUID shunted by C_1). The resonances of this circuit, denoted a, b, and c, tune with the SQUID flux, as shown in Fig. 1. Throughout this work, we use the SQUID as a tunable linear coupling element, neglecting the intrinsic nonlinearity of the SQUID. To understand the origin of the bilinear coupling between the three modes, one can consider the energy stored in the

SQUID, $E_{\text{SQ}} \propto L_{\text{SQ}}I_{\text{SQ}}^2$. For each mode j, a fraction α_j of the mode current I_j flows through the SQUID such that $I_{\text{SQ}} = \sum_j \alpha_j I_j$. This results in $E_{\text{SQ}} \propto \sum_{j,k} \alpha_j \alpha_k L_{\text{SQ}} I_j I_k$, effectively producing linear coupling of the modes j and k.

APPENDIX B: THEORY OF PARAMETRICALLY COUPLED MODES

In this section, we describe our approach to solving the EOMs for a system of parametrically coupled modes. We aim at deriving the resulting scattering parameters (Appendixes B 1–B 4) and output noise (Appendix B 5). We begin with the case of a single damped and driven oscillator to introduce the concepts and our notation. We then describe the building blocks of parametric physics, namely, frequency conversion and amplification between two modes. Combining these processes in three-mode systems allows us to describe the circulator and the directional amplifier. We largely reproduce the concepts and style from Ranzani and Aumentado [16], with minor changes of notation and normalization.

1. A single driven and damped oscillator

The Hamiltonian for a driven harmonic oscillator with resonant frequency ω_a and a loss rate κ_a, after tracing over bath modes in the rotating-wave approximation, is

$$\frac{\hat{\mathcal{H}}}{\hbar} = \left(\omega_a - i\frac{\kappa_a}{2}\right)\hat{a}^\dagger\hat{a} + i\sqrt{\kappa_a^{\text{ext}}}(\hat{a}_{\text{in}} - \hat{a}_{\text{in}}^\dagger)(\hat{a} + \hat{a}^\dagger), \quad \text{(B1)}$$

where κ_a^{ext} is the external coupling to the drive port, and $\hat{a}$ and $\hat{a}_{\text{in}}$ are the time-dependent annihilation operators for the internal mode and the input drive, respectively. To simplify the notation, we choose (1) to include the loss as an imaginary component of the resonant frequency, making the Hamiltonian non-Hermitian and (2) to have the phase quadrature of the drive coupled to the amplitude quadrature of the internal mode. Note that, to preserve quantum commutators, Eq. (B1) needs an extra noise input term proportional to $\sqrt{\kappa_a^{\text{int}}}$, so that $\kappa_a = \kappa_a^{\text{ext}} + \kappa_a^{\text{int}}$ (see Appendix B 4).

The Heisenberg-Langevin EOM is $\dot{\hat{a}} = -i[\hat{a}, \hat{\mathcal{H}}/\hbar]$. To analyze the EOM, we consider an input signal at the signal frequency ω_a^s and move to a rotating frame at that frequency by redefining the annihilation operators $\hat{a} \rightarrow \hat{a}\exp(-i\omega_a^s t)$ and $\hat{a}_{\text{in}} \rightarrow \hat{a}_{\text{in}}\exp(-i\omega_a^s t)$, so that $\hat{a}$ and $\hat{a}_{\text{in}}$ are time independent in this frame. Additionally, we will study the dynamics of the expectation values, defining $a \equiv \langle\hat{a}\rangle$. The equation of motion reads

$$\kappa_a \Delta_a a = i\sqrt{\kappa_a^{\text{ext}}}a_{\text{in}}, \quad \text{(B2)}$$

where

$$\Delta_a = \frac{\omega_a^s - \omega_a}{\kappa_a} + \frac{i}{2} \quad \text{(B3)}$$

is a normalized complex detuning parameter. In the above, we apply the rotating-wave approximation (RWA), neglecting a term with explicit time dependence in the signal frame. We assume that the frequency of this term, $2\omega_a^s$, is much larger than the relevant linewidth of the oscillator, κ_a, so that the susceptibility, $\chi = i/(\kappa_a \Delta_a)$, at those frequencies is small enough to not cause any appreciable dynamics.

To introduce the graph representation that we will use in the following cases, Fig. 7(c) shows the graph corresponding to the single-oscillator EOM (B2). It consists of a single vertex for the mode amplitude a, with a *self-loop* associated with the complex detuning Δ_a.

The output field at the signal frequency ω_a^s is obtained via the input-output relation $a_{\text{out}} = \sqrt{\kappa_a^{\text{ext}}}a - a_{\text{in}}$, finally leading to the familiar Lorentzian form of the reflection coefficient:

$$S_{aa} = \frac{a_{\text{out}}}{a_{\text{in}}} = \left(\frac{\kappa_a^{\text{ext}}}{\kappa_a}\frac{i}{\Delta_a} - 1\right). \quad \text{(B4)}$$

2. Two coupled modes

Let us now consider two oscillators with resonant frequencies ω_a and ω_b, loss rates κ_a and κ_b, and a time-dependent coupling rate $g_{ab}(t) = |g_{ab}|\cos(\omega_{ab}^p t + \phi_{ab})$. The Hamiltonian of the system is

$$\begin{aligned}\hat{\mathcal{H}}/\hbar = &\left(\omega_a - i\frac{\kappa_a}{2}\right)\hat{a}^\dagger\hat{a} + i\sqrt{\kappa_a^{\text{ext}}}(\hat{a}_{\text{in}} - \hat{a}_{\text{in}}^\dagger)(\hat{a} + \hat{a}^\dagger)\\ &+ \left(\omega_b - i\frac{\kappa_b}{2}\right)\hat{b}^\dagger\hat{b} + i\sqrt{\kappa_b^{\text{ext}}}(\hat{b}_{\text{in}} - \hat{b}_{\text{in}}^\dagger)(\hat{b} + \hat{b}^\dagger)\\ &- g_{ab}(t)(\hat{a} + \hat{a}^\dagger)(\hat{b} + \hat{b}^\dagger), \quad \text{(B5)}\end{aligned}$$

where κ_a^{ext} and κ_b^{ext} are the coupling rates to the external port, and $\hat{a}$, $\hat{b}$, $\hat{a}_{\text{in}}$, and $\hat{b}_{\text{in}}$ are the time-dependent annihilation operators for the internal mode and input drives for each oscillator, respectively. We consider the oscillators to be driven at the frequencies ω_a^s and ω_b^s, related to each other by the pump frequency of ω_{ab}^p. We move to a corotating frame and redefine the (time-independent) annihilation operators $\hat{a} \rightarrow \hat{a}\exp(-i\omega_a^s t)$, $\hat{b} \rightarrow \hat{b}\exp(-i\omega_b^s t)$, $\hat{a}_{\text{in}} \rightarrow \hat{a}_{\text{in}}\exp(-i\omega_a^s t)$, and $\hat{b}_{\text{in}} \rightarrow \hat{b}_{\text{in}}\exp(-i\omega_b^s t)$.

In the case of resonant coupling, g_{ab} is time independent, so $\omega_a^s = \omega_b^s$. In this case, if the two oscillators are detuned from one another ($|\omega_b - \omega_a| \gg \kappa_a, \kappa_b$), then the large detuning (small susceptibility) prevents appreciable energy transfer between the oscillators. If the pump frequency is near the sum or difference of the two resonant frequencies, however, then both detunings can be small (with a corresponding large susceptibility) to allow energy transfer
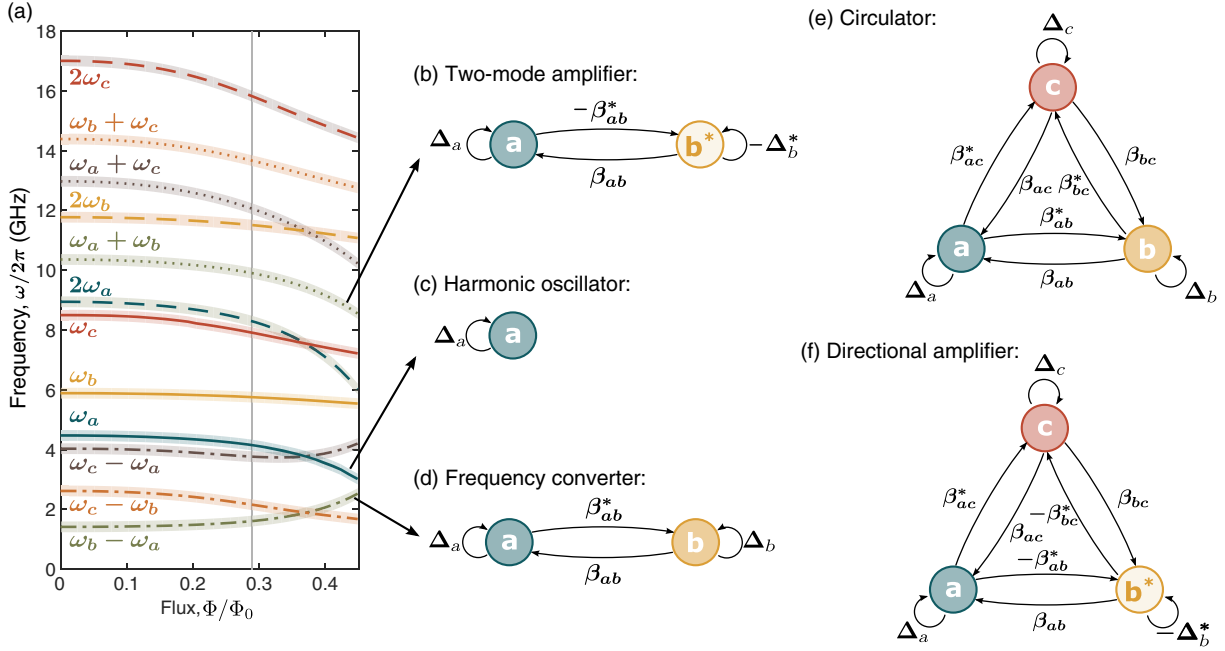
FIG. 7.   Process spectroscopy. (a) Mode frequencies ω_j, and first-order modulation frequencies $|\omega_j \pm \omega_k|$ (j, $k \in \{a, b, c\}$) as a function of flux. The shaded areas represent a bandwidth of 180 MHz, necessary to ensure a good rotating-wave approximation. Graph representation of the EOM for (b) parametric amplification between two modes, (c) a single harmonic oscillator, (d) frequency conversion between two modes, (e) circulation, and (f) directional phase-preserving amplification.

between the two oscillators. When $\omega_{ab}^p \approx |\omega_b - \omega_a|$, a pump photon can bridge the energy gap between the two oscillators allowing for frequency conversion. When $\omega_{ab}^p \approx \omega_a + \omega_b$, a pump photon can be down-converted into a photon in each oscillator, amplifying each oscillator's amplitude.

a. Frequency conversion

Consider the case where the coupling term is modulated near the difference frequency $\omega_{ab}^p \approx |\omega_b - \omega_a|$. To simplify the notation, let us choose $\omega_b > \omega_a$, such that $\omega_b^s = \omega_a^s + \omega_{ab}^p$. The EOMs after the RWA become

$$\kappa_a \Delta_a a + \sqrt{\kappa_a \kappa_b} \beta_{ab} b = i\sqrt{\kappa_a^{\text{ext}}} a_{\text{in}},$$

$$\kappa_b \Delta_b b + \sqrt{\kappa_a \kappa_b} \beta_{ab}^* a = i\sqrt{\kappa_b^{\text{ext}}} b_{\text{in}}, \qquad (B6)$$

where $\Delta_j = (\omega_j^s - \omega_j)/\kappa_j + i/2$ are normalized complex detunings, and $\beta_{ab} = |g_{ab}|e^{i\phi_{ab}}/(2\sqrt{\kappa_a \kappa_b})$ is the normalized complex coupling between the mode amplitudes a and b.

When working with multiple modes, it becomes useful to adopt a matrix representation of these equations. We define a vector of intracavity mode amplitudes $\mathbf{A} = (a, b)^T$, input mode amplitudes $\mathbf{A}_{\text{in}} = (a_{\text{in}}, b_{\text{in}})^T$, output mode amplitudes $\mathbf{A}_{\text{out}} = (a_{\text{out}}, b_{\text{out}})^T$, diagonal matrices for the total loss rates $\mathbf{K} = \text{diag}(\sqrt{\kappa_a}, \sqrt{\kappa_b})$, and external couplings $\mathbf{K}^{\text{ext}} = \text{diag}(\sqrt{\kappa_a^{\text{ext}}}, \sqrt{\kappa_b^{\text{ext}}})$, and, finally, the mode-coupling

matrix $\mathbf{M}$, so that Eq. (B6) becomes $\mathbf{KMKA} = i\mathbf{K}^{\text{ext}}\mathbf{A}_{\text{in}}$, where

$$\mathbf{M} = \begin{pmatrix} \Delta_a & \beta_{ab} \\ \beta_{ab}^* & \Delta_b \end{pmatrix}. \qquad (B7)$$

The graph representation of the mode-coupling matrix $\mathbf{M}$ is shown in Fig. 7(d). Each vertex corresponds to a mode amplitude, with self-loops associated with the complex detuning Δ_j. The vertices are connected by coupling edges associated with the coupling terms β_{ab} and β_{ab}^*.

We can solve these EOMs to calculate the scattering matrix $\mathbf{S} = \mathbf{A}_{\text{out}}/\mathbf{A}_{\text{in}}{}^T$, resulting in

$$\mathbf{S} = i\mathbf{HM}^{-1}\mathbf{H} - \mathbb{1}, \qquad (B8)$$

where we introduce the matrix $\mathbf{H} = \text{diag}(\sqrt{\eta_a}, \sqrt{\eta_b})$, where $\eta_j = \kappa_j^{\text{ext}}/\kappa_j$ are coupling efficiency parameters characterizing the degree to which each mode is overcoupled. Expanding Eq. (B8) results in

$$\mathbf{S} = \begin{pmatrix} \dfrac{i\eta_a \Delta_b}{\Delta_a \Delta_b - |\beta_{ab}|^2} - 1 & \dfrac{-i\sqrt{\eta_a \eta_b}\beta_{ab}}{\Delta_a \Delta_b - |\beta_{ab}|^2} \\[2ex] \dfrac{-i\sqrt{\eta_a \eta_b}\beta_{ab}^*}{\Delta_a \Delta_b - |\beta_{ab}|^2} & \dfrac{i\eta_b \Delta_a}{\Delta_a \Delta_b - |\beta_{ab}|^2} - 1 \end{pmatrix}. \qquad (B9)$$

On resonance ($\Delta_j = i/2$) and neglecting internal loss ($\eta_j = 1$), one recovers Eq. (3):

$$\mathbf{S} = \begin{pmatrix} \frac{1-4|\beta_{ab}|^2}{1+4|\beta_{ab}|^2} & \frac{4i\beta_{ab}}{1+4|\beta_{ab}|^2} \\ \frac{4i\beta_{ab}^*}{1+4|\beta_{ab}|^2} & \frac{1-4|\beta_{ab}|^2}{1+4|\beta_{ab}|^2} \end{pmatrix}.$$

Unity transmission coincides with impedance matching (zero reflection) for $|\beta_{ab}| = 1/2$. Note that, when β_{ab} is complex, $S_{ab} \neq S_{ba}$ (although $|S_{ab}| = |S_{ba}|$). However, for modes at different frequencies, the phase shift between S_{ab} and S_{ba} must be measured relative to a reference whose phase is arbitrary. In a two-mode system, there can always be found a reference phase such that β_{ab} is real and $\mathbf{S}$ is reciprocal. Yet, the phase dependence of $\mathbf{S}$ will become crucial when discussing three-mode systems, in which the phase reference is built into the system. Finally, note that, for resonant coupling, where β_{ab} is required to be real, the scattering matrix is unambiguously reciprocal.

b. Parametric amplification

We now consider the case where the coupling is modulated near the sum frequency $\omega_{ab}^p \approx \omega_a + \omega_b$, such that $\omega_b^s = \omega_{ab}^p - \omega_a^s$. The EOMs after applying the RWA become

$$\kappa_a \Delta_a a + \sqrt{\kappa_a \kappa_b}\beta_{ab} b^* = i\sqrt{\kappa_a^{\mathrm{ext}}} a_{\mathrm{in}},$$

$$-\kappa_b \Delta_b^* b^* - \sqrt{\kappa_a \kappa_b}\beta_{ab}^* a = i\sqrt{\kappa_b^{\mathrm{ext}}} b_{\mathrm{in}}^*, \qquad \text{(B10)}$$

or, in the matrix form $\mathbf{KMKA} = i\mathbf{K}^{\mathrm{ext}}\mathbf{A}_{\mathrm{in}}$, where

$$\mathbf{M} = \begin{pmatrix} \Delta_a & \beta_{ab} \\ -\beta_{ab}^* & -\Delta_b^* \end{pmatrix}, \qquad \text{(B11)}$$

and $\mathbf{A} = (a, b^*)^T$, $\mathbf{A}_{\mathrm{in}} = (a_{\mathrm{in}}, b_{\mathrm{in}}^*)^T$, $\mathbf{A}_{\mathrm{out}} = (a_{\mathrm{out}}, b_{\mathrm{out}}^*)^T$. Here, note that, for parametric amplification, $\beta_{ab} = |g_{ab}|e^{-i\phi_{ab}}/(2\sqrt{\kappa_a \kappa_b})$, where the sign of the phase comes from the convention in Eq. (B5). The corresponding graph representation is shown in Fig. 7(b). When making a comparison to the EOMs for the frequency conversion (B6), one notices three differences: (1) the mode amplitude a is now coupled to the conjugate-mode amplitude b^*, (2) the complex detuning term for the conjugate mode is conjugated and with a minus sign, and (3) the coupling term for the conjugate mode has a minus sign. These subtle differences lead to the following scattering matrix:

$$\mathbf{S} = \begin{pmatrix} \frac{i\eta_a \Delta_b^*}{\Delta_a \Delta_b^* - |\beta_{ab}|^2} - 1 & \frac{i\sqrt{\eta_a \eta_b}\beta_{ab}}{\Delta_a \Delta_b^* - |\beta_{ab}|^2} \\ \frac{-i\sqrt{\eta_a \eta_b}\beta_{ab}^*}{\Delta_a \Delta_b^* - |\beta_{ab}|^2} & \frac{-i\eta_b \Delta_a}{\Delta_a \Delta_b^* - |\beta_{ab}|^2} - 1 \end{pmatrix}. \qquad \text{(B12)}$$

On resonance $(\Delta_j = i/2)$ and neglecting internal loss $(\eta_j = 1)$, we recover Eq. (5):

$$\mathbf{S} = \begin{pmatrix} \frac{1+4|\beta_{ab}|^2}{1-4|\beta_{ab}|^2} & \frac{4i\beta_{ab}}{1-4|\beta_{ab}|^2} \\ \frac{-4i\beta_{ab}^*}{1-4|\beta_{ab}|^2} & \frac{1+4|\beta_{ab}|^2}{1-4|\beta_{ab}|^2} \end{pmatrix}.$$

The scattering parameters diverge for $|\beta_{ab}| = 1/2$, in stark contrast to the frequency-conversion case. In the limit $|\beta_{ab}| \to 1/2^-$, each scattering parameter has an amplitude gain, $\sqrt{G} \approx 2/(1 - 4|\beta_{ab}|^2)$. Similar to the frequency-conversion case, we observe $S_{ab} \neq S_{ba}$ for β_{ab} complex.

3. Three-mode systems

Parametric frequency conversion and parametric amplification are the building blocks from which we can construct complex coupled-mode networks. Both processes exhibit a directional phase shift, which is the first ingredient for building nonreciprocal devices like isolators and circulators. The second ingredient required is an interferometer to unambiguously define the reference phase. Here, we will build such an interferometer in frequency space by parametrically coupling three modes to form a loop. We will use the matrix formalism and its graph counterpart, which become very useful when extending the mode basis to three or more modes. Indeed, the coupling network is well captured by the mode-coupling matrix $\mathbf{M}$ alone. Let us now consider three oscillators with resonant frequencies ω_j and loss rates κ_j, driven at the signal frequencies ω_j^s, for $j \in \{a, b, c\}$.

a. Circulation

To build a circulator, we will connect these three modes via frequency conversion. For that, we simultaneously modulate the coupling between the modes at the difference frequencies $\omega_{ab}^p \approx |\omega_b - \omega_a|$, $\omega_{bc}^p \approx |\omega_c - \omega_b|$, and $\omega_{ac}^p \approx |\omega_a - \omega_c|$, satisfying the condition $\omega_{ab}^p + \omega_{bc}^p = \omega_{ac}^p$. The resulting equations of motion for the internal modes $\mathbf{A} = (a, b, c)^T$ are described by the mode-coupling matrix

$$\mathbf{M} = \begin{pmatrix} \Delta_a & \beta_{ab} & \beta_{ac} \\ \beta_{ab}^* & \Delta_b & \beta_{bc} \\ \beta_{ac}^* & \beta_{bc}^* & \Delta_c \end{pmatrix}, \qquad \text{(B13)}$$

where $\Delta_j = (\omega_j^s - \omega_j)/\kappa_j + i/2$ is the complex detuning for mode j, and $\beta_{jk} = |g_{jk}|e^{i\phi_{jk}}/(2\sqrt{\kappa_j \kappa_k})$ is the normalized coupling between the modes j and k. The graph representation of this Langevin matrix is shown in Fig. 7(e), which highlights the loop structure of the coupling network. Each pair of modes is now coupled via two different paths. These couplings lead to interference, controlled by the loop phase $\phi_{\mathrm{loop}} = \phi_{ab} + \phi_{bc} - \phi_{ac}$. Solving for the scattering matrix using Eq. (B8), we obtain

$$\mathbf{S} = \begin{pmatrix} i\eta_a \frac{\Delta_b\Delta_c - |\beta_{bc}|^2}{|\mathbf{M}|} - 1 & i\sqrt{\eta_a\eta_b}\frac{\beta_{ac}\beta_{bc}^* - \beta_{ab}\Delta_c}{|\mathbf{M}|} & i\sqrt{\eta_a\eta_c}\frac{\beta_{ab}\beta_{bc} - \beta_{ac}\Delta_b}{|\mathbf{M}|} \\ i\sqrt{\eta_a\eta_b}\frac{\beta_{ac}^*\beta_{bc} - \beta_{ab}^*\Delta_c}{|\mathbf{M}|} & i\eta_b\frac{\Delta_a\Delta_c - |\beta_{ac}|^2}{|\mathbf{M}|} - 1 & i\sqrt{\eta_b\eta_c}\frac{\beta_{ab}^*\beta_{ac} - \beta_{bc}\Delta_a}{|\mathbf{M}|} \\ i\sqrt{\eta_a\eta_c}\frac{\beta_{ab}^*\beta_{bc}^* - \beta_{ac}^*\Delta_b}{|\mathbf{M}|} & i\sqrt{\eta_b\eta_c}\frac{\beta_{ab}\beta_{ac}^* - \beta_{bc}^*\Delta_a}{|\mathbf{M}|} & i\eta_c\frac{\Delta_a\Delta_b - |\beta_{ab}|^2}{|\mathbf{M}|} - 1 \end{pmatrix}, \tag{B14}$$

where $|\mathbf{M}| = \Delta_a\Delta_b\Delta_c - |\beta_{bc}|^2\Delta_a - |\beta_{ac}|^2\Delta_b - |\beta_{ab}|^2\Delta_c + 2|\beta_{ab}||\beta_{bc}||\beta_{ac}|\cos\phi_{\text{loop}}$. Importantly, compared to the two-mode cases, the *magnitudes* of the scattering parameters are now nonreciprocal, $|S_{ij}| \neq |S_{ji}|$, for $\phi_{\text{loop}} \neq 0, \pi$. Maximum isolation from mode b to mode a ($S_{ab} = 0$) is achieved for $\beta_{ac}\beta_{bc}^* = \beta_{ab}\Delta_c$. On resonance ($\Delta_j = i/2$) and neglecting internal loss ($\eta_j = 1$), this condition coincides with unity transmission from a to b, $|S_{ba}| = 1$, for $|\beta_{ab}| = |\beta_{bc}| = |\beta_{ac}| = 1/2$ and for a loop phase $\phi_{\text{loop}} = -\pi/2$. Setting $\phi_{ab} = \phi_{bc} = -\phi_{ac} = \pi/2$, one recovers the ideal circulator scattering matrix from Eq. (7):

$$\mathbf{S} = \begin{pmatrix} 0 & 0 & 1 \\ 1 & 0 & 0 \\ 0 & 1 & 0 \end{pmatrix}.$$

In Fig. 8, we show the measured and simulated scattering parameters as a function of the total loop phase ϕ_{loop} for the FPJA operating as a circulator. Excellent agreement is found between data and theory. For the opposite loop phase, $\phi_{\text{loop}} = \pi/2$, the direction of circulation is reversed. Additionally, one can recover reciprocal scattering parameters for $\phi_{\text{loop}} = 0$ and $\phi_{\text{loop}} = \pi$.

b. Directional phase-preserving amplification

To build a directional amplifier, we will connect two pairs of modes via amplification and close the interferometer using frequency conversion. For that, we simultaneously modulate the coupling between the modes at the frequencies $\omega_{ab}^p \approx \omega_a^s + \omega_b^s$, $\omega_{bc}^p \approx \omega_b^s + \omega_c^s$, and $\omega_{ac}^p \approx |\omega_a^s - \omega_c^s|$, satisfying the condition $\omega_{ac}^p + \omega_{ab}^p = \omega_{bc}^p$. The resulting equations of motion for the internal modes $\mathbf{A} = (a, b^*, c)^T$ are described by the matrix
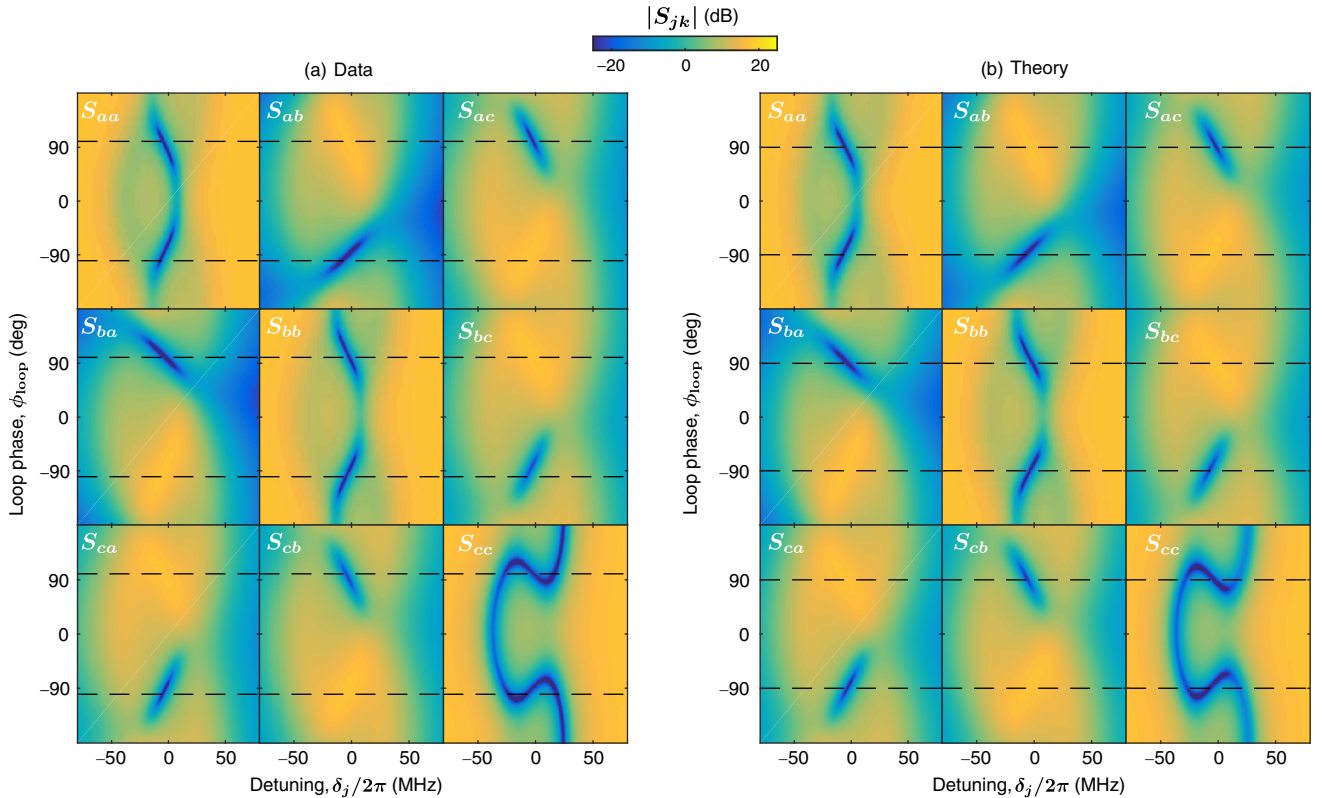

FIG. 8.   Circulator. Magnitude of the (a) measured and (b) simulated scattering parameters as a function of the loop phase ϕ_{loop} for near-ideal pump strengths.

$$\mathbf{M} = \begin{pmatrix} \Delta_a & \beta_{ab} & \beta_{ac} \\ -\beta_{ab}^* & -\Delta_b^* & \beta_{bc} \\ \beta_{ac}^* & -\beta_{bc}^* & \Delta_c \end{pmatrix}. \tag{B15}$$

The detuning and coupling terms for the frequency-conversion and amplification processes are defined using the same convention as in the two-mode cases, with $\Delta_j = (\omega_j^s - \omega_j)/\kappa_j + i/2$, $\beta_{ac} = |g_{ac}|e^{i\phi_{ac}}/(2\sqrt{\kappa_a\kappa_c})$, and $\beta_{jk} = |g_{jk}|e^{-i\phi_{jk}}/(2\sqrt{\kappa_j\kappa_k})$, where $j, k \in \{b, c\}$. The graph representation of this mode-coupling matrix is shown in Fig. 7(f), again forming an interferometer. Solving for the scattering matrix using Eq. (B8), we obtain

$$\mathbf{S} = \begin{pmatrix} i\eta_a \frac{|\beta_{bc}|^2 - \Delta_b^*\Delta_c}{|\mathbf{M}|} - 1 & i\sqrt{\eta_a\eta_b}\frac{-\beta_{ab}\Delta_c - \beta_{ac}\beta_{bc}^*}{|\mathbf{M}|} & i\sqrt{\eta_a\eta_c}\frac{\beta_{ac}\Delta_b^* + \beta_{ab}\beta_{bc}}{|\mathbf{M}|} \\ i\sqrt{\eta_a\eta_b}\frac{\beta_{ab}^*\Delta_c + \beta_{ac}^*\beta_{bc}}{|\mathbf{M}|} & i\eta_b\frac{\Delta_a\Delta_c - |\beta_{ac}|^2}{|\mathbf{M}|} - 1 & i\sqrt{\eta_b\eta_c}\frac{-\beta_{bc}\Delta_a - \beta_{ab}^*\beta_{ac}}{|\mathbf{M}|} \\ i\sqrt{\eta_a\eta_c}\frac{\beta_{ac}^*\Delta_b^* + \beta_{ab}^*\beta_{bc}^*}{|\mathbf{M}|} & i\sqrt{\eta_b\eta_c}\frac{\beta_{bc}^*\Delta_a + \beta_{ab}\beta_{ac}^*}{|\mathbf{M}|} & i\eta_c\frac{|\beta_{ab}|^2 - \Delta_a\Delta_b^*}{|\mathbf{M}|} - 1 \end{pmatrix}, \tag{B16}$$

where $|\mathbf{M}| = -\Delta_a\Delta_b^*\Delta_c + |\beta_{bc}|^2\Delta_a + |\beta_{ac}|^2\Delta_b^* + |\beta_{ab}|^2\Delta_c + 2|\beta_{ab}||\beta_{bc}||\beta_{ac}|\cos\phi_{\text{loop}}$ and $\phi_{\text{loop}} = \phi_{ab} + \phi_{bc} + \phi_{ac}$. Similar to the circulation case, the magnitude of the scattering parameters are nonreciprocal. The condition for maximum isolation from port b to port a, $S_{ab} = 0$, is achieved for $\beta_{ac}\beta_{bc}^* = -\beta_{ab}\Delta_c$. On resonance, this condition leads to a loop phase $\phi_{\text{loop}} = -\pi/2$. We further neglect internal loss and require an input match $|S_{aa}| = 0$ on resonance, which can be accomplished by choosing the matching condition for the frequency-conversion branch ($|\beta_{ac}| = 1/2$) and letting the two amplification branches be equal $|\beta_{ab}| = |\beta_{bc}|$. To fix the phases of the scattering-matrix elements, we choose $\phi_{ab} = \phi_{ac} = -\phi_{bc} = -\pi/2$ to arrive at the scattering matrix of Eq. (9):

$$\mathbf{S} = \begin{pmatrix} 0 & 0 & 1 \\ \sqrt{G-1} & \sqrt{G} & 0 \\ \sqrt{G} & \sqrt{G-1} & 0 \end{pmatrix},$$

where $\sqrt{G} = (1 + 4|\beta_{ab}|^2)/(1 - 4|\beta_{ab}|^2)$. Let us consider a coherent signal at the input of mode a, while modes b and c are seeded by vacuum fluctuations. Both the signal in mode a and the vacuum fluctuations in mode b are amplified toward modes b and c. This leads to the same minimum system noise as a standard two-mode amplifier. Finally, the vacuum fluctuations in c are routed to mode a with unity gain. The direction of the amplification is reversed for $\phi_{\text{loop}} = \pi/2$, and one recovers reciprocal scattering parameters for $\phi_{\text{loop}} = 0$ and $\phi_{\text{loop}} = \pi$. The measured and simulated scattering parameters as a function of the total loop phase ϕ_{loop} for FPJA operation as a directional amplifier are shown in Fig. 9. Excellent agreement is found between data and theory for $|\phi_{\text{loop}}| \gtrsim 80$. The return loss and isolation are very sensitive to the perfect interference between all coupling branches, i.e., to the pump strengths and detunings. In addition, at high gain, higher-order nonlinearities such as self-Kerr and cross-Kerr nonlinearity require us to manually adjust the pumps. More careful tuning would, in principle, allow us to increase the isolation and return losses, here on the order of 10 dB.

For $|\phi_{\text{loop}}| \lesssim 80$ deg, the system undergoes free oscillations. While the free oscillation threshold is simply $|\beta_{ab}| = 1/2$ for a two-mode amplifier [see Eq. (B12)], the threshold for a three-mode directional amplifier becomes phase dependent. A general method to calculate whether the system will freely oscillate is to look for signal frequency solutions of $|\mathbf{M}| = 0$ with a positive imaginary part.

4. Generalization to multiple input and output ports per mode

In this section, we generalize the formalism to include multiple input ports for each mode, crucial for accurate noise calculation in the next section.

In Appendixes B 1–B 3, we consider each mode j to be coupled to a single external port and account for internal loss using the coupling efficiency parameter $\eta_j = \kappa_j^{\text{ext}}/\kappa_j$. This method is sufficient for calculating the scattering parameters between the external ports of interest. However, to describe a system with multiple external (or internal) ports per mode, and also to reach accurate noise calculations, one needs to generalize this formalism. Intuitively, if a fraction of the input signal can be lost in the environment, then, conversely, noise from this environment enters the system. In other words, in order to preserve the commutators of the input and output fields, one must account for all of the ports contributing to the total loss rates of each mode.

The generalization to multiple ports per mode consists of a straightforward redefinition of the input and output field, $\mathbf{A}_{\text{in}}$ and $\mathbf{A}_{\text{out}}$, and of the matrix $\mathbf{H}$. Note that, because the network of coupled internal modes stays unchanged, the mode-coupling matrix $\mathbf{M}$ does as well. Each mode j can be coupled to multiple ports (which can include "ports" to the thermal environment), so that $\kappa_j = \sum_k \kappa_j^k$, where k indexes all ports to which mode j is coupled. For a system
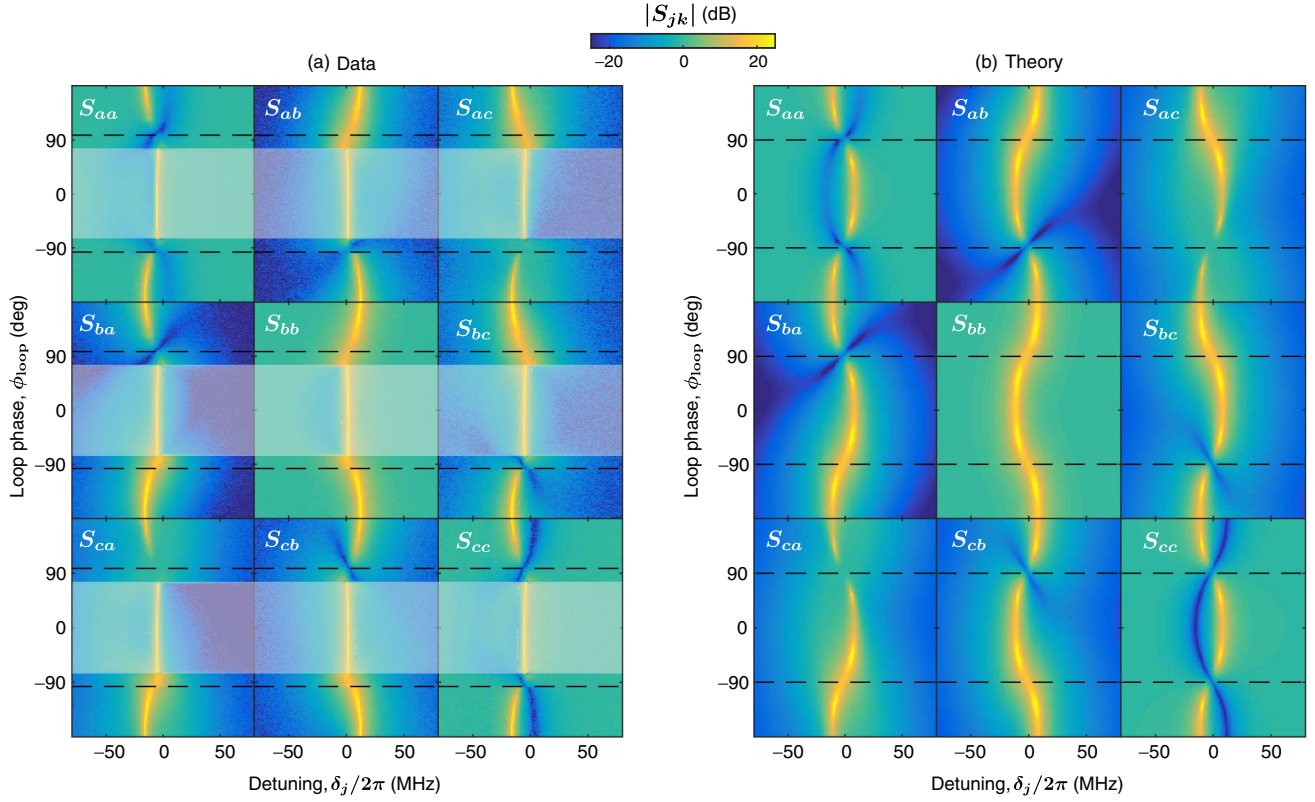
FIG. 9. Directional phase-preserving amplifier. Magnitude of the (a) measured and (b) simulated scattering parameters as a function of the loop phase ϕ_{loop} for near-ideal pump strengths. In practice, the device undergoes free oscillations for $|\phi_{\text{loop}}| \lesssim 80$ deg (see Appendix B 3).

of n modes coupled to a total of m ports, $\mathbf{A}_{\text{in}}$ and $\mathbf{A}_{\text{out}}$ become vectors of length m, $\mathbf{H}$ becomes a matrix of size $n \times m$ where $H_{jk} = \sqrt{\eta_j^k}$, and $\mathbf{M}$ remains a matrix of size $n \times n$. The condition $\sum_k \eta_j^k = 1$ ensures that all noise sources are accounted for. Equation (B8) becomes

$$\mathbf{S} = i\mathbf{H}^T\mathbf{M}^{-1}\mathbf{H} - \mathbb{1}. \tag{B17}$$

As an example, we consider the directional amplifier shown in Appendix B 3 a and include a single additional port per mode to describe the coupling to the environment at a rate κ_j^{int}, so that $\kappa_j = \kappa_j^{\text{ext}} + \kappa_j^{\text{int}}$. We define the input field as $\mathbf{A}_{\text{in}} = (\hat{a}_{\text{in}}, \hat{\xi}_{a,\text{in}}^\dagger, \hat{b}_{\text{in}}^\dagger, \hat{\xi}_{b,\text{in}}^\dagger, \hat{c}_{\text{in}}, \hat{\xi}_{c,\text{in}})^T$, where $\hat{\xi}_{j,\text{in}}$ is the input field for the environment of mode j. Similarly, we define $\mathbf{A}_{\text{out}} = (\hat{a}_{\text{out}}, \hat{\xi}_{a,\text{out}}, \hat{b}_{\text{out}}^\dagger, \hat{\xi}_{b,\text{out}}^\dagger, \hat{c}_{\text{out}}, \hat{\xi}_{c,\text{out}})^T$. The matrix $\mathbf{H}$ becomes

$$\mathbf{H} = \begin{pmatrix} \sqrt{\eta_a^{\text{ext}}} & \sqrt{\eta_a^{\text{int}}} & 0 & 0 & 0 & 0 \\ 0 & 0 & \sqrt{\eta_b^{\text{ext}}} & \sqrt{\eta_b^{\text{int}}} & 0 & 0 \\ 0 & 0 & 0 & 0 & \sqrt{\eta_c^{\text{ext}}} & \sqrt{\eta_c^{\text{int}}} \end{pmatrix}.$$

5. Output noise

In this section, we use the generalized scattering parameters [Eq. (B17)] to calculate the output noise of a system of parametrically coupled modes. The quantum-noise spectral density of the output fields [33], $\mathcal{N}[\omega]$, is defined as the diagonal elements of the covariance matrix of the output fields, $\langle \mathbf{A}_{\text{out}}^\dagger[\omega']\mathbf{A}_{\text{out}}^T[\omega]\rangle/2\pi\delta(\omega - \omega')$, in units of photons. One can then express the spectral density of the output field using the relation between the input and output covariance matrix:

$$\langle \mathbf{A}_{\text{out}}^\dagger[\omega']\mathbf{A}_{\text{out}}^T[\omega]\rangle = \mathbf{S}^*[\omega']\langle \mathbf{A}_{\text{in}}^\dagger[\omega']\mathbf{A}_{\text{in}}^T[\omega]\rangle\mathbf{S}^T[\omega]. \tag{B18}$$

The input covariance matrix contains all of the information about the input noise, including bath temperatures or correlations, and can describe both classical and non-classical noise sources. For example, if the environment of mode j is in a thermal state, the corresponding input noise follows $\langle \hat{\xi}_{j,\text{in}}^\dagger[\omega']\hat{\xi}_{j,\text{in}}[\omega]\rangle = 2\pi n_{j,\text{th}}\delta(\omega - \omega')$ and $\langle \hat{\xi}_{j,\text{in}}[\omega]\hat{\xi}_{j,\text{in}}^\dagger[\omega']\rangle = 2\pi(n_{j,\text{in}} + 1)\delta(\omega - \omega')$, where $n_{j,\text{th}} = [\exp(\hbar\omega_j/k_BT) - 1]^{-1}$ is the mean thermal occupation number at the resonator frequency ω_j at a temperature T (k_B is the Boltzmann constant).

Note that, in this work, we perform linear measurements of the output field quadratures. Therefore, we access the symmetrized (classical) spectral density [33], $\overline{\mathcal{N}}[\omega]$:

$$\overline{\mathcal{N}}[\omega] = \frac{1}{2}(\mathcal{N}[\omega] + \mathcal{N}[-\omega]). \qquad (B19)$$

The theoretical predictions for the output noise made in Figs. 3(e), 5(f), and 5(g) are based on our best guess for the scattering parameters, shown in Figs. 3(d) and 5(d), and we assume that each port is seeded by vacuum noise.

6. Discussion

The agreement between theory and experiment is primarily due to a clean mode basis. Indeed, the EOMs rely on the rotating-wave approximation to eliminate dynamics at any spurious frequencies. If the approximation cannot be made, new modes appear in the coupled network, leading, for example, to losses or added noise. The device presented here is carefully designed so that all first-order parametric processes can be separated by frequency. In Fig. 7(a), we show the mode frequencies ω_j and all of the modulation frequencies $|\omega_j \pm \omega_k|$ for $j, k \in \{a, b, c\}$ as a function of flux. The shaded areas represent a bandwidth 3 times larger than the largest mode width $(3\kappa_c/2\pi = 180 \text{ MHz})$,

necessary to ensure a good rotating-wave approximation. At the flux bias chosen in this work, $\Phi/\Phi_0 \approx 0.29$, all of these processes are well separated.

APPENDIX C: SYSTEM NOISE CALIBRATION

The calibration of the noise performance of an amplifier at millikelvin temperature and close to the standard quantum limit is not a trivial task. Most commonly used is the so-called Y-factor method. It requires a calibrated noise source, such as a variable-temperature resistor [18], a circuit QED system [27], or a biased metallic tunnel junction [19,34]. While each technique is subject to various experimental and conceptual challenges, all techniques share a common problem: they calibrate the system-added noise to a reference plane that is usually not the one of the amplifier. For a simplistic but concrete and general example, consider that the noise source and the amplifier are connected by a transmission line with unknown loss: the calibrated noise at the output of the source is now uncalibrated at the input of the amplifier. This fact leads to the following general consideration when calibrating the noise of an amplifier: all components necessary for the proper operation of the amplifier (circulators, filters, couplers, cables, etc.) should be included in the system noise calibration.
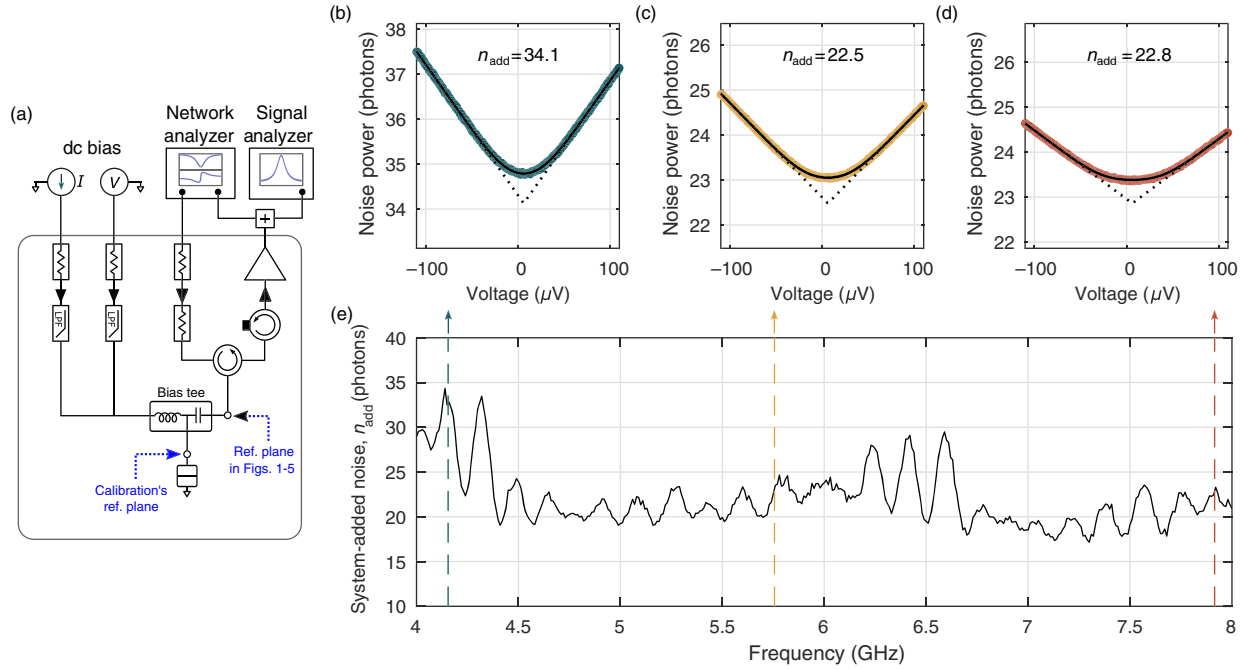

FIG. 10.   Noise calibration. (a) The noise emitted by a biased metallic tunnel junction is measured using the same setup as for the FPJA (LPF: low-pass filter). (b)–(d) Measured power spectral density in photon unit as a function of the voltage across the shot-noise junction, measured at the frequencies $\omega_1/2\pi = 4.155$ GHz, $\omega_2/2\pi = 5.756$ GHz, and $\omega_3/2\pi = 7.915$ GHz, corresponding to the resonances of the FPJA shown in Fig. 1(c). The solid black lines are a fit to Eq. (C2). The dashed lines are linear extrapolations of the noise at high voltage, and their crossing point corresponds to the system-added noise. (e) Measured system-added noise as a function of frequency.

In this work, we choose a slightly different approach. In a separate cooldown, we replace the FPJA by a metallic tunnel junction and a bias tee, leaving every other component of the measurement chain the same (including the HEMT amplifier bias parameters), as shown in Fig. 10(a). This allows for the calibration of the system noise down to the junction's reference plane, which differs from the FPJA reference plane only by the loss of the bias tee (<0.5 dB). We therefore obtain an upper bound for the system noise temperature at the reference plane of the FPJA.

The power spectral density of the noise emitted by a metalic tunnel junction, at a frequency ω and a temperature T, as a function of the voltage V across the junction is $\mathcal{N} = \mathcal{N}_+ + \mathcal{N}_-$ (unit of quanta s^{-1} Hz^{-1}), where

$$\mathcal{N}_{\pm} = \frac{k_B T}{2\hbar\omega}\left[\frac{eV \pm \hbar\omega}{2k_B T}\coth\left(\frac{eV \pm \hbar\omega}{2k_B T}\right)\right], \quad \text{(C1)}$$

where k_B is the Boltzmann constant, e is the electron charge, and $\hbar$ is the reduced Planck constant. The gain of the full measurement chain, G_{sys}, and the noise *added* by that chain, n_{add} (unit of quanta), is extracted from the measured power spectral density, $\mathcal{N}_{\text{meas}}$, following

$$\mathcal{N}_{\text{meas}} = G_{\text{sys}}(\mathcal{N} + n_{\text{add}}). \quad \text{(C2)}$$

The power spectral density in photon units, $\mathcal{N}_{\text{meas}}/G_{\text{sys}}$, measured at the frequencies $\omega_1/2\pi = 4.155$ GHz, $\omega_2/2\pi = 5.756$ GHz, and $\omega_3/2\pi = 7.915$ GHz, corresponding to the resonance of the FPJA, are shown, respectively, in Figs. 10(b), 10(c), and 10(d). From a fit to Eq. (C2), we extract a constant temperature of 100 mK and a system-added noise of $n_{\text{add}} = 34.1$, 22.5, and 22.8, respectively, at ω_1, ω_2, and ω_3. Similar measurements are performed over the 4- to 8-GHz band, and the measured system noise as a function of frequency is shown in Fig. 10. One can see oscillations due to slight impedance mismatches and component imperfections throughout the chain. The temperature is consistently measured at 100 mK, probably due to the imperfect thermalization of the sample box.

---

[1] M. H. Devoret and R. J. Schoelkopf, Superconducting circuits for quantum information: An outlook, Science **339**, 1169 (2013).

[2] M. Aspelmeyer, T. J. Kippenberg, and F. Marquardt, Cavity optomechanics, Rev. Mod. Phys. **86**, 1391 (2014).

[3] R. Barends *et al.*, Superconducting quantum circuits at the surface code threshold for fault tolerance, Nature (London) **508**, 500 (2014).

[4] L. Sun, A. Petrenko, Z. Leghtas, B. Vlastakis, G. Kirchmair, K. M. Sliwa, A. Narla, M. Hatridge, S. Shankar, J. Blumoff, L. Frunzio, M. Mirrahimi, M. H. Devoret, and R. J. Schoelkopf, Tracking photon jumps with repeated quantum non-demolition parity measurements, Nature (London) **511**, 444 (2014).

[5] R. Vijay, C. Macklin, D. H. Slichter, S. J. Weber, K. W. Murch, R. Naik, A. N. Korotkov, and I. Siddiqi, Stabilizing Rabi oscillations in a superconducting qubit using quantumfeedback, Nature (London) **490**, 77 (2012).

[6] D. Ristè, M. Dukalski, C. A. Watson, G. de Lange, M. J. Tiggelman, Ya. M. Blanter, K. W. Lehnert, R. N. Schouten, and L. DiCarlo, Deterministic entanglement of superconducting qubits by parity measurement and feedback, Nature (London) **502**, 350 (2013).

[7] D. J. Wilson, V. Sudhir, N. Piro, R. Schilling, A. Ghadimi, and T. J. Kippenberg, Measurement-based control of a mechanical oscillator at its thermal decoherence rate, Nature (London) **524**, 325 (2015).

[8] K. W. Murch, S. J. Weber, C. Macklin, and I. Siddiqi, Observing single quantum trajectories of a superconducting qubit, Nature (London) **502**, 211 (2011).

[9] J. D. Teufel, T. Donner, M. A. Castellanos-Beltran, J. W. Harlow, and K. W. Lehnert, Nanomechanical motion measured with an imprecision below that at the standard quantum limit, Nat. Nanotechnol. **4**, 820 (2009).

[10] N. Roch, M. E. Schwartz, F. Motzoi, C. Macklin, R. Vijay, A. W. Eddins, A. N. Korotkov, K. B. Whaley, M. Sarova, and I. Siddiqi, Observation of Measurement-Induced Entanglement and Quantum Trajectories of Remote Superconducting Qubits, Phys. Rev. Lett. **112**, 170501 (2014).

[11] H. J. Kimble, The quantum internet, Nature (London) **453**, 1023 (2008).

[12] B. Yurke, M. L. Roukes, R. Movshovich, and A. N. Pargellis, A low-noise series-array Josephson junction parametric amplifier, Appl. Phys. Lett. **69**, 3078 (1996).

[13] M. A. Castellanos-Beltran, K. D. Irwin, G. C. Hilton, L. R. Vale, and K. W. Lehnert, Amplification and squeezing of quantum noise with a tunable Josephson metamaterial, Nat. Phys. **4**, 929 (2008).

[14] N. Bergeal, F. Schackert, M. Metcalfe, R. Vijay, V. E. Manucharyan, L. Frunzio, D. E. Prober, R. J. Schoelkopf, S. M. Girvin, and M. H. Devoret, Phase-preserving amplification near the quantum limit with a Josephson ring modulator, Nature (London) **465**, 64 (2010).

[15] L. Deák and T. Fülöp, Reciprocity in quantum, electromagnetic and other wave scattering, Ann. Phys. (Amsterdam) **327**, 1050 (2012).

[16] L. Ranzani and J. Aumentado, Graph-based analysis of nonreciprocity in coupled-mode systems, New J. Phys. **17**, 023024 (2015).

[17] A. Metelmann and A. A. Clerk, Nonreciprocal Photon Transmission and Amplification via Reservoir Engineering, Phys. Rev. X **5**, 021025 (2015).

[18] W. F. Kindel, M. D. Schroer, and K. W. Lehnert, Generation and efficient measurement of single photons from fixed-frequency superconducting qubits, Phys. Rev. A **93**, 033817 (2016).

[19] N. Roch, E. Flurin, F. Nguyen, P. Morfin, P. Campagne-Ibarcq, M. H. Devoret, and B. Huard, Widely Tunable, Nondegenerate Three-Wave Mixing Microwave Device Operating near the Quantum Limit, Phys. Rev. Lett. **108**, 147701 (2012).

[20] A. Kamal, J. Clarke, and M. H. Devoret, Noiseless non-reciprocity in a parametric active device, Nat. Phys. **7**, 311 (2011).

[21] A. Kamal, A. Roy, J. Clarke, and M. H. Devoret, Asymmetric Frequency Conversion in Nonlinear Systems Driven by a Biharmonic Pump, Phys. Rev. Lett. **113**, 247003 (2014).

[22] B. Abdo, K. Sliwa, L. Frunzio, and M. Devoret, Directional Amplification with a Josephson Circuit, Phys. Rev. X **3**, 031001 (2013).

[23] B. Abdo, K. Sliwa, S. Shankar, M. Hatridge, L. Frunzio, R. Schoelkopf, and M. Devoret, Josephson Directional Amplifier for Quantum Measurement of Superconducting Circuits, Phys. Rev. Lett. **112**, 167701 (2014).

[24] J. Kerckhoff, K. Lalumière, B. J. Chapman, A. Blais, and K. W. Lehnert, On-Chip Superconducting Microwave Circulator from Synthetic Rotation, Phys. Rev. Applied **4**, 034002 (2015).

[25] N. A. Estep, D. L. Sounas, J. Soric, and A. Alù, Magnetic-free non-reciprocity and isolation based on parametrically modulated coupled-resonator loops, Nat. Phys. **10**, 923 (2014).

[26] K. M. Sliwa, M. Hatridge, A. Narla, S. Shankar, L. Frunzio, R. J. Schoelkopf, and M. H. Devoret, Reconfigurable Josephson Circulator/Directional Amplifier, Phys. Rev. X **5**, 041020 (2015).

[27] C. Macklin, K. O'Brien, D. Hover, M. E. Schwartz, V. Bolkhovsky, X. Zhang, W. D. Oliver, and I. Siddiqi, A near-quantum-limited Josephson traveling-wave parametric amplifier, Science **350**, 307 (2015).

[28] W. H. Louisell, *Coupled Mode and Parametric Electronics* (John Wiley & Sons, New York, 1960).

[29] A. J. Sirois, M. A. Castellanos-Beltran, M. P. DeFeo, L. Ranzani, F. Lecocq, R. W. Simmonds, J. D. Teufel, and J. Aumentado, Coherent-state storage and retrieval between superconducting cavities using parametric frequency conversion, Appl. Phys. Lett. **106**, 172603 (2015).

[30] D. M. Pozar, *Microwave Engineering, 4th Edition* (Wiley, New York, 2012).

[31] P. T. Leung and K. Young, Gauge invariance and reciprocity in quantum mechanics, Phys. Rev. A **81**, 032107 (2010).

[32] H. Heffner, Gain, band width, and noise characteristics of the variable-parameter amplifier, J. Appl. Phys. **29**, 1321 (1958).

[33] A. A. Clerk, M. H. Devoret, S. M. Girvin, F. Marquardt, and R. J. Schoelkopf, Introduction to quantum noise, measurement, and amplification, Rev. Mod. Phys. **82**, 1155 (2010).

[34] L. Spietz, K. W. Lehnert, I. Siddiqi, and R. J. Schoelkopf, Primary electronic thermometry using the shot noise of a tunnel junction, Science **300**, 1929 (2003).